Physiological and morphological studies on cerebellar synapses of $Ca_V2.1$ mutant mice rocker

Takashi Kodama

DOCTOR OF PHILOSOPHY

Department of Physiological Sciences

School of Life Science

The Graduate University for Advanced Studies

2006

CONTENTS

Abstract

The *rocker* mice are hereditary ataxic mutants, which carry a point mutation in the gene encoding the $Ca_V2.1$ (P/Q-type) Ca^{2+} channel α_1 subunit. They show the mildest phenotypes among the reported $Ca_V2.1$ mutant mice, allowing us to evaluate primary symptoms caused by the $Ca_V2.1$ dysfunction. Although the basic properties of the *rocker* mutant channel have been reported, their influence on physiological functions remains unclear. Here, I studied the impacts of the *rocker* mutant Ca^{2+} channel on synaptic transmission especially in cerebellar Purkinje cells, where $Ca_V2.1$ Ca^{2+} channel mediates a major activity-dependent Ca^{2+} influx. Despite of the small changes in channel function, synaptic transmission in the parallel fiber (PF)-Purkinje cell (PC) synapses was severely impaired, whereas the climbing fiber inputs onto PCs appeared to function normally. I further explored the origin of the transmission impairment in the PF-PC synapses in *rocker* mice. Presynaptic functions of the PF-PC synapses, however, were unexpectedly normal in terms of paired-pulse facilitation, sensitivity to extracellular Ca^{2+} concentration, and glutamate concentration in synaptic clefts. Electron microscopic analyses including freeze-fracture replica labeling revealed that both the number and density of postsynaptic AMPA (α-amino-3-hydroxy-5-methyl-4-isoxazole propionic acid) receptors substantially

decreased without gross structural changes of the PF-PC synapses. I also observed an abnormal arborization of PC dendrites in young adult *rocker* mice (≈1 month of age). These lines of evidence suggest that the *rocker* mutation exerts its influence especially on postsynaptic structures and functions in the PF-PC synapses.

Introduction

Voltage-dependent calcium channels (VDCCs) serve cells, especially neurons, a depolarization-dependent Ca^{2+} entry, which enables them to respond to electric signals in diverse ways including regenerative excitation known as Ca^{2+} spikes, neurotransmitter release, and regulation of gene expression (for reviews, see Catterall, 1998; Schneggenburger & Neher, 2005). VDCCs are, at the molecular level, composed of a main α_1 subunit and auxiliary subunits including the α_2/δ and β subunits (Catterall., 1998). The α_1 subunit is the principal subunit of VDCCs, incorporating the conduction pore, the voltage sensor and gating apparatus, and sites of channel regulation by second messengers, drugs, and toxins. Mammalian α_1 subunits are encoded by at least ten distinct genes (Ertel et al., 2000).

To explore subtype-specific VDCC functions, analysis of VDCC mutant mice is one of frequently used strategies (Jun et al., 1999; Ino et al., 2001; Sochivko et al., 2002). However, since the VDCCs participate in a variety of cellular functions, their dysfunction would cause directly or indirectly different symptoms, which makes it difficult to understand the causal relationship between the VDCC dysfunction and the phenotypes. To appreciate primary effects of the VDCC dysfunction, thus, comprehensive studies of mutant mice that suffer from a milder VDCC dysfunction

would be fruitful, because its phenotypes are expected to be simpler and limited. Moreover, it could reveal some common pathogenetic mechanisms underlying human neurological diseases attributable to the VDCC dysfunction including familial hemiplegic migraine, episodic ataxia-2 (Ophoff et al., 1996), and spinocerebellar ataxia-6 (Zhuchenko et al., 1997).

In this study, I report the primary influence of the $Ca_V2.1$ (P/Q-type) Ca^{2+} channel mutation *rocker* (*rkr*; Zwingman et al., 2001) especially on synaptic transmission in cerebellar cortex. The *rkr* mutation, which was induced by ethylnitrosourea mutagenesis, results in a single amino acid exchange (T1310K) located between the hydrophobic regions 5 and 6 in the third homologous domain of the $Ca_V2.1$ $\alpha 1$ subunit. Among the strains of $Ca_V2.1$ mutant mice, *rkr* mice show the mildest phenotypes: relatively moderate ataxia and absence seizure, but no paroxysmal dyskinesia. It has already been demonstrated that the influence of the *rkr* mutation on the $Ca_V2.1$ channel function is relatively mild: in acutely dissociated Purkinje cell somas, reduction of the Ca^{2+} channel current density to 80% of normal without any substantial changes in voltage-dependency and kinetics of gating (Itsukaichi et al, 2002). Dendrites of cerebellar Purkinje cells (PCs) of *rkr* mice show a “weeping willow” appearance in the second year of life (Zwingman et al., 2001), but abnormalities commonly found in PCs

of other $Ca_V2.1$ mutant mice, including ectopic spines, axonal torpedoes, and aberrant expression of tyrosine hydroxylase, are not observed. Recently Stahl et al. (2004, 2005) reported the abnormal oculomotor behavior in *rkr* mice, but basic information of the *rkr* mutation, i.e., the influence of the mutation on synapses remains unknown. Here, I report the salient influence of the *rkr* mutation on synaptic transmission in the parallel fiber-Purkinje cell synapses rather than the climbing fiber-Purkinje cell synapses, and proposed the physiological process primarily affected by the $Ca_V2.1$ dysfunction.

Experimental procedures

Animals

All experiments described herein were reviewed and approved by the Animal Care and Use Committee of the National Institute for Physiological Sciences (Okazaki, Japan), and were performed according to the institutional guidelines concerning the care and handling of experimental animals. The C57BL/6J-*Os* +/+ *Cacna1a*^{rkr} strain of *rkr* mice were introduced from the Jackson Laboratory (Bar Harbor, ME). Control normal animals of C57BL/6Cr Slc strain were purchased from Nihon SCL (Hamamatsu, Japan). The mice were provided with a commercial diet (CE-2; Nihon Clea, Tokyo, Japan) and water ad libitum with controlled temperature, humidity, and lighting (22 ± 2°C, 55 ± 5%, and 12 hr light / dark cycle with lights on at 7 A.M.). The *rkr* strain was maintained and propagated mainly through the heterozygous intercrosses. Here, homozygous mice of *rkr* are simply referred to as "*rkr* mice", in which all analyses have been carried out.

Genotyping

The genotypes of *rkr* mice can be inferred by the oligosyndactylism phenotype (*Os*): embryonic lethal for +/+, reduced finger number for *rkr*/+, and normal finger number for *rkr*/*rkr*. Although *Os* is tightly linked with *Cacna1a*, recombination between

Cacna1a^{rkr} and *Os*, which leads to an error in *rkr* genotyping, is possible. Thus, I verified the genotype of the mice used for breeding by PCR. Normal *Cacna1a* and *Cacna1a*^{rkr} alleles were distinctively detected by the PCR using the primer pairs, rkr-2 (5'-CTCATAGACTTTATGTGTGG-3') and Crkr20 (5'-GAACTCCTTGGACTCGTCCG-3'), and rkr-2 and Arkr21 (5'-CGAACTCCTTGGACTCGTCCT-3'), respectively, both of which produced a 430-bp DNA fragment. The conditions of both reactions consisted of 5 min at 94°C, and 45 cycles of 1 min at 94°C, 1 min at 62°C and 1 min at 72°C, with a final extension for 7 min at 72°C.

Slice preparation and whole-cell patch clamp recording of EPSCs

Brains of P13-15 or P22-32 mice were quickly removed and cooled in ice-cold artificial CSF (ACSF) containing (in mM): 125 NaCl, 2.5 KCl, 1.25 NaH_2PO_4, 2 $CaCl_2$, 1 $MgCl_2$, 25 $NaHCO_3$, and 25 glucose, saturated with carbogen. Parasagittal 250-μm-thick slices were cut from the cerebellar vermis with a microslicer (DTK-1000; Dosaka, Kyoto, Japan) in ice-cold ACSF. After slicing, slices were incubated at room temperature at least for 1 hr in ACSF.

After incubation, slices were transferred to a recording chamber and perfused with

ACSF at a rate of 1-2 ml/min. Bicuculline methochloride (10 μM; Tocris Cookson, Avonmouth, UK) was always added to the perfusate to eliminate spontaneous IPSCs. Patch pipettes were made from borosilicate or alminosilicate capillaries (outer diameter: 1.5 mm; Hilgenberg, Malsfeld, Germany). The resistance of patch pipettes was 2-5 MΩ when filled with an intracellular solution containing (in mM): 100 Cs-gluconate, 34.5 CsCl, 4 NaCl, 10 HEPES, 4 Mg-ATP, 0.3 Na-GTP, 10 EGTA (adjusted to pH 7.3 with CsOH). QX-314 (final 5 mM; Sigma-Aldrich, St. Louis, MO) was added to prevent Na^+ spike generation. Calculated liquid junction potential was -12.6 mV and was not corrected for. PCs were visually identified using an upright microscope (BX50WI; Olympus Optical, Tokyo, Japan) equipped with an infrared differential interference contrast video system (Hamamatsu Photonics, Hamamatsu, Japan). Whole cell voltage-clamp recordings were obtained from PCs in the culmen (lobules 4 and 5), unless otherwise specified. The pipette series resistance (Rs) was compensated by 50%-90%. Cells were rejected if Rs increased above 15 MΩ. EPSCs were recorded with an EPC9 patch-clamp amplifier (HEKA Elektronik, Lambrecht, Germany). Stimulation and data acquisition were performed by using PULSE program (HEKA Elektronik). The signals were serially filtered at 10 kHz (-3dB) by a 3-pole Bessel filter and at 3 kHz (-3dB) by a 4-pole Bessel filter. Signals were usually digitized at 20 or 40 kHz. The

recordings were performed at a bath temperature of 30-32°C unless otherwise specified.

Parallel fiber response

When quantifying the amplitude of parallel fiber-mediated EPSCs (PF-EPSCs), I used a large concentric electrode (50 μm in diameter of center tip) for stimulation, which was moved along the pial surface and placed where a maximum response was evoked. With this configuration, I could minimize the variation of the response derived from the position of the stimulus electrode. Single square pulses of 100-μs duration and amplitude ranging from 5 to 20 μA were applied at 0.2 Hz. When a large current was evoked abruptly, which was presumably derived from direct stimulation of dendrites or climbing fibers, I terminated the recording, and excluded the result from statistical examination. The holding potential was –70 mV. Records taken under a low Rs condition (<10 MΩ, compensated for up to 90%) were used in analyses of the EPSC kinetics. The values of EPSC peak amplitude, 10-90% rise time, and decay time constant were obtained by averaging the values from 3-5 consecutive traces. The decaying phase of EPSCs was fit with a single exponential to determine the decay time constant.

When evaluating the sensitivity to external Ca^{2+} concentration ($[Ca^{2+}]_e$) and

γ-D-glutamylglycine (γ-DGG; Tocris Cookson) blockade effect on PF-EPSCs, I used a glass pipette (2-3 MΩ) filled with ACSF or a concentric electrode for stimulation. Stimulations were applied at 0.05 Hz. I monitored Rs throughout the recording by applying short negative voltage pulse (-5 mV from holding potential for 5 ms), and recordings were discarded when Rs varied by >20%. I also excluded the recordings in which an average of response after washout varied by > 15% of the original baseline. The experiments using γ-DGG were conducted under room temperature to facilitate long stable recording. When changing $[Ca^{2+}]_e$, I maintained the total divalent concentration (4 mM) by adjusting the external Mg^{2+} concentration ($[Mg^{2+}]_e$): $[Ca^{2+}]_e$ and $[Mg^{2+}]_e$ (mM) were 2 and 2 for control solution, 1 and 3 for low $[Ca^{2+}]_e$ solution, and 3 and 1 for high $[Ca^{2+}]_e$ solution, respectively.

Climbing fiber response

Climbing fiber-mediated EPSCs (CF-EPSCs) were evoked by electrical stimulation, using a bipolar theta-shaped capillary electrode (tip diameter: 7-14 μm) filled with 1M NaCl or a glass pipette (2-3 MΩ) filled with ACSF. The pipette was placed in the granule cell layer around a soma of the recorded PCs. Square pulses of 100-μsec duration and amplitude ranging from 5 to 20 μA were applied at 0.1 Hz, unless

otherwise specified. CF-EPSCs were identified by its emergence of all-or-none fashion under peri-threshold stimulus intensity and the nature of paired-pulse depression. When assessing innervation of multiple CFs onto PCs, I surveyed PCs in lobule 2 to 9 at room temperature by moving the stimulus electrode systematically by 20-μm step, and increasing the stimulus intensity to 50 μA gradually at each stimulation site. I excluded PCs with multiple innervations from the analysis of CF-EPSC conductance and kinetics. The recordings taken at –10 or 0 mV of a holding potential under the low Rs condition (<12 MΩ, compensated for up to 90%) were used for the analyses of the EPSCs kinetics. I checked a shift of the voltage offset value between before and after recording, and corrected command voltages with it.

Complex spikes were evoked by the same method as above and recorded in the current-clamp mode. Because PCs continuously fired in a native condition, I injected negative holding currents (-100 – -300 pA) to stabilize the membrane potential around –65 mV. I rejected cells, when PCs did not reach < -63 mV of membrane potential by the holding current injection, or did not show overshooting action potential (> 20 mV). I analyzed complex spikes in terms of spike number, plateau potential, and after-hyperpolarization. Plateau potential was defined as the difference between the resting potential and the potential 25 ms after stimulation. After-hyperpolarization was

defined as the difference between the resting potential and the negative peak of potential after spike generation. The values were calculated by averaging measurements from 10 – 30 traces.

SDS-digested freeze-fracture replica-labeling

Mice (P25-30) were anesthetized with pentobarbital (200 mg/kg of body weight, i.p.), and transcardially fixed with 0.5% paraformaldehyde and 15% saturated picric acid solution in 0.1 M phosphate buffer (pH 7.4, 4°C). Parasagittal sections (150 μm) were cut with a microslicer (Linearslicer PRO7; Dosaka), and the lobule 4 and 5 was cut out. The trimmed section were cryoprotected with 30% glycerol in 0.1 M phosphate buffer (PB) overnight at 4°C, and quickly frozen by a high pressure freeze machine (HPM010; BAL-TEC, Balzers, Liechtenstein). The frozen samples were then freeze-fractured, and replicated with carbon (5 nm), shadowed by platinum (2 nm), and again replicated with carbon (15-20 nm) in BAF 060 (BAL-TEC). After thawing, tissue debris attached to the replicas was digested with gentle stirring at 80°C overnight in the following solution: 15 mM Tris[hydroxymethyl]aminomethane (Tris), 20% sucrose, and 2.5% sodium dodecyl sulfate. The replicas were then washed 3 times with the washing buffer (0.1% Tween-20, 0.05% BSA, 0.05% NaN_3 in Tris buffered saline), and reacted with a pan-AMPA

receptor (GluR1-4) antibody (3.8 μg/ml) (Nusser et al., 1998; Tanaka et al., 2005) at 15°C overnight, followed by incubation with an antibody against the glutamate receptor δ2 subunit (GluRδ2) (0.55 μg/ml) at 37°C for 1 hr. Both antibodies were designed to bind extracellular domains of the proteins. GluRδ2 antibody was generated in a guinea pig as described in Hirai (2001). After several washes with washing buffer, the replicas were reacted with an anti-rabbit IgG coupled to 5-nm gold particles (for pan-AMPA receptor) and an anti-guinea pig IgG coupled to 10-nm or 15-nm gold particles (for GluRδ2) (British Biocell International, Cardiff, UK) at 37°C for 1hr. The replicas were examined with an electron microscope (EM208S; FEI, Eindhoven, The Netherlands) and photographed at a magnification of 71,000×. Immunogold particles for AMPA receptors were counted in excitatory postsynaptic areas of the PF-PC synapses indicated by clusters of intramembrane particles (IMP clusters) on the exoplasmic fracture-face (E-face) that had immunogold particles for GluRδ2 within or nearby (Harris & Landis, 1986). We tried different criteria for the number of GluRδ2 labels with which we accepted the IMP clusters as the PF-PC synapses, and all criteria we tested gave similar results on AMPA receptor quantification. Therefore, we accepted IMP clusters with at least one GluRδ2 label as the PF-PC synapses for statistical analyses. The length of measurements was calibrated by a grating replica (Ted Pella, Redding, CA).

Electron microscopy

For quantitative analyses by conventional electron microscopy, mice (P24-32) were anesthetized with pentobarbital (200 mg/kg of body weight, i.p.), and transcardially fixed with 2% paraformaldehyde, 0.6 % glutaraldehyde and 0.2% picric acid in 0.05 M PB (pH 7.4, 4°C) or Karnovsky fixative. Microslicer sections (50 μm) were postfixed with 1% osmium tetroxide in 0.1 M PB for 25 min and 1% uranyl acetate for 35 min, dehydrated in graded ethanols and propylene oxide, and embedded in Durcupan resin (Fluka, Bucks, Switzerland). Ultrathin sections cut in the parasagittal plane were prepared from upper third of the molecular layer (ML) of the lobules 4 and 5, stained with 2% uranyl acetate for 10 min and Reynolds lead citrate staining solution for 10 min, examined with an electron microscope (EM208S), and photographed at a magnification of 6,300× for measurement of the synapse density and 13,000× for the three-dimensional reconstruction of the synapses. For quantification of the density of the PF-PC synapses, I used the physical disector method (Sterio, 1983; Coggeshall & Lekan, 1996). Briefly, I prepared two serial sections (70 nm thick) from upper third of the ML of the lobules 4 and 5, and counted the number of the synapses that appeared in one section but disappear in the other section, which gave me the estimation of the

number of the synapses per a volume. Three-dimensional reconstruction of the PF-PC synapses was carried out by using Reconstruct (http://synapses.bu.edu/tools/). The PF-PC synapses were morphologically identified as asymmetric synapses on spines. The length of measurements was calibrated by a grating replica (Ted Pella).

Immunohistochemistry

All processes were conducted under room temperature, unless otherwise specified. Mice at P22-29 were anesthetized with pentobarbital (200 mg/kg of body weight, i.p.), perfused transcardially with the fixative containing 4% paraformaldehyde and 0.2% picric acid in phosphate-buffered saline (PBS). After excision from the skull, brains were further immersed overnight in the same fixative at 4°C and processed for preparation of parasagittal 10 μm-thick sections of the cerebellum with a cryostat microtome (CM3050S; Leica Microsystems, Nussloch, Germany). A midsagittal section was selected from each mouse such that the section had the smallest medullar zone at the base of the cerebellar lobules. The sections were sequentially treated with PBS containing 0.3% Triton X-100 for 15 min, with PBS containing 50 mM glycine for 15 min, with PBS containing 5% bovine serum alubmin and 3% normal goat serum for 1 hr (blocking), and then incubated overnight at 4°C with rabbit anti-calbindin D-28K

antibody (Chemicon, Temecula, CA) at a dilution of 1:500. After several washes with PBS, sections were incubated with 4 μg/ml Alexa Fluor 555 goat anti-rabbit IgG (Invitrogen, Carlsbad, CA) for 1 hr. Signals were acquired by a confocal laser-scanning microscope (CLSM, LSM510; Carl Zeiss, Oberkochen, Germany) as an image stacks containing a volume of 225.3×225.3×10 μm^3. The density of PCs was estimated by counting the number of PC nuclei in the volume of the image stacks taken from middle straight portions of the lobule 4 and 5.

Retrograde labeling of PCs

Under anesthesia with chloral hydrate (300 mg/kg of body weight, i.p.) or ketamine (200 mg/kg of body weight, i.m.), a glass pipette (tip diameter, ≈30 μm) filled with 10% phosphate buffered saline (PBS) solution of biotinylated dextran amine (10,000 MW; Invitrogen) was inserted stereotaxically to the right cerebellar fastigial nucleus of mice at P29-32 (Sugihara et al., 1999). The tracer was injected by air pressure at 10 psi for 50 ms with 5 s intervals by Pneumatic PicoPump (PV820; World Precision Instruments, Sarasota, FL). I injected 0.1-0.2 μl of the tracer in total. Pipettes were left in situ for 5 min after injection before withdrawal. 4-5 days after injection, mice were anesthetized with pentobarbital (200 mg/kg of body weight, i.p.), and transcardially fixed with 2%

paraformaldehyde, 0.6 % glutaraldehyde and 0.2% picric acid in 0.05 M PB (pH 7.4, 4°C). Dissected brains were kept in the same fixative overnight at 4°C. Parasagittal 50-μm-thick sections were cut from the cerebellar vermis with a microslicer, treated with 0.5% Triton X-100 in PBS for 15 min and incubated with 10 μg/ml Alexa Fluor 488 conjugated streptavidin (Invitrogen) and 0.5% Triton X-100 in PBS for 30 min. For morphometric analyses, image stacks containing whole dendrites and soma of the PCs were taken with CLSM. I obtained the image stacks from all PCs in straight portions of lobules 4, 5 and 6 that were well-isolated from others and had intact dendrites. To remove noises from images, I first applied "*Seed Fill*" method of IgorPro (version 5.1, Wavemetrics, Lake Oswego, OR), and, then, manually treated images using ImageJ (http://rsb.info.nih.gov/ij/). I produced the projections of the image stacks vertical to the plane of PCs (z-projections) in which all the further morphometries were carried out. To examine the extent of the dendritic arborization in the ML, I used a grid of parallel lines spaced evenly from the apical boundary of PC soma to the pia (i.e. from 0% to 100% of ML in my definition), and aligned parallel to the pia. Intersections between these lines and the dendritic branches were counted. I also quantified the total dendrite length for each cell with aid of Neuron J, a plugin program running on ImageJ (Meijering et al., 2004). To compare the density of spines on the PC dendrites, I collected image stacks

from the most distal dendrites with strong signal in lobules 4 and 5 at higher magnification (1024 * 1024 pixels in scanning area of 20.5 * 20.5 μm for each image), and determined the density of spines in the z-projections of the image stacks. I regarded the structure protruding aside from the dendrites as a spine, and ignore those located on the "top" or "bottom" of the dendrites that could not be distinguished in the z-projection images. Thus my quantification inevitably resulted in underestimation, but allowed me to evaluate the difference between normal and *rkr* mice.

In vivo recording

Under anesthesia with urethane (1.0 mg/g of body weight, i.p.), a mouse (1-8 months of age) was mounted on the stereotaxic holder (SR-6N; Narishige, Tokyo, Japan)without prevention of free respiration. The rectal temperature was maintained between 37 and 38°C with a heating pad. The depth of anesthesia was monitored by assessing the animals' responsiveness in terms of eye blinks. The head position was adjusted so that the heights of the lambda and bregma skull points were equal. A small window (diameter: < 1 mm) was opened at the skull over crus I (coordination: 2.5 mm posterior to lambda, 2.5 mm lateral to the midline), and a silicon ring made by cutting a silicon tube (outer diameter: 7 mm, inside diameter: 5 mm) into 3-4 mm height was cemented

around the window to make a recording chamber. To record unit firings extracellularly, a glass electrode filled with 0.5 M NaCl (15-30 MΩ) was inserted through the skull window at an angle of 0-15°anterior to vertical line by pulse motor-driven micromanipulator (SM-21; Narishige). As a reference electrode, an AgCl electrode was placed under the skin of the back. During recording, the chamber on the skull was filled with 4% agarose in PBS to stabilize the electrode position. An air puff stimulation (40 psi, 20 ms) was controlled by pneumatic picopump (PV820; World Precision Instruments, Sarasota, FL), and delivered to the ipsilateral perioral surface by a glass pipe (inside diameter 0.87 mm). The tip was located 1 cm away from the skin of the whisker region at a lateral angle of 45° with respect to the midline of the head. Signals were amplified with Axoclamp 2A amplifier (Molecular Devices, Palo Alto, CA), band-pass filtered at 300-3k Hz, and digitized at 20 kHz with a CED 1401plus (Cambridge Electronic Design, Cambridge, England). Recording and stimulation were controlled by Spike2 software (Cambridge Electronic Design).

Chemicals

Peptide toxin ω-Aga IVA was purchased from Peptide Institute (Osaka, Japan). All other chemicals were from Nacalai Tesque (Kyoto, Japan), or Wako Pure Chemical Industries

(Osaka, Japan), unless otherwise specified.

Data analysis and statistics

All values were given as means ± SEM, unless otherwise stated. Data analyses and fitting procedures were performed by IgorPro. Statistical significance was assessed by an unpaired *t*-test, unless otherwise stated. For multiple comparisons, a repeated ANOVA was performed, followed by Bonferroni test for all pairwise comparisons (* $p<0.05$; ** $p<0.01$; *** $p<0.001$). Statistical analyses were performed by SPSS (version 12.0, SPSS, Chicago, IL).

Results

In mammalian CNS, the $Ca_V2.1$ Ca^{2+} channel plays a major role in neurotransmitter release at synapses. Their contribution to presynaptic Ca^{2+} influx has been well characterized especially in two types of the excitatory synapse onto PCs: synapses with parallel fibers (PFs) and climbing fibers (CF) (Regehr & Mintz, 1994; Mintz et al., 1995). Moreover, the $Ca_V2.1$ channel prominently mediates an activity-dependent Ca^{2+} influx in PCs (for review, Hartmann & Konnerth, 2005). Thus, the *rkr* mutation was expected to cause some alterations in the synaptic transmission in PCs. To assess the impact of the *rkr* mutation on synaptic transmission, I recorded PF-mediated EPSCs (PF-EPSCs) and CF-mediated EPSCs (CF-EPSCs) by whole-cell patch-clamp recording in parasagittal cerebellar slices from *rkr* mice.

EPSCs at parallel fiber-Purkinje cell synapses in rkr mice

I first examined PF-EPSCs using whole-cell voltage clamp in cerebellar slices from *rkr* mice at P23-26 when obvious ataxia starts to be observed. I evoked PF-EPSCs by electric stimulation with a large-tip (50 μm in diameter) concentric electrode. I moved the electrode along the pial surface and placed it where a maximum response was obtained. I chose this configuration because, by exciting PFs in a large area, it

minimized the variation of the EPSC amplitude derived from the stimulus location. With increments of the stimulus intensity, the peak amplitude of PF-EPSCs increased almost linearly in both normal and *rkr* mice (Fig. 1B, D). However, PF stimulation was significantly less effective in eliciting PF-EPSCs in *rkr* mice than normal mice, with the stimulation of the intensity ranging from 12.5 to 20 μA ($p < 0.05$). The mean amplitude of the EPSCs at 17.5 μA of stimulation was 1.24 ± 0.12 nA for normal mice and 0.38 ± 0.07 nA for *rkr* mice, indicating a severe reduction of PF-EPSCs to 31% of normal.

To examine the developmental time course of the impairment, I also recorded PF-EPSCs in *rkr* mice at P13-15 when an obvious ataxia was not seen. Although the amplitudes of PF-EPSCs in *rkr* mice at this age exhibited a variation among cells (Fig. 1A right), the averages of them was significantly different from the normal value in the stimulation intensity range from 12.5 to 20 μA (Fig. 1C; $p < 0.01$). The mean amplitudes of the EPSCs at 17.5 μA of stimulation were 1.51 ± 0.14 nA for the normal mice, and 0.80 ± 0.14 nA for *rkr* mice, indicating the milder reduction of PF-EPSCs to 53% of normal. These results indicated that the impairment of the PF-PC synaptic transmission had been apparent since young age (P13-15), and progressed by P23-26.

To assess the kinetics of PF-EPSCs, I measured the decay time constant and the 10-90% rise time on the traces obtained at the maximal stimulus intensity (10-20 μA). Statistical

test revealed that both parameters were not significantly different between normal and *rkr* PCs of the same age (see Table 1).

EPSCs at climbing fiber-Purkinje cell synapses in rkr mice

Next, I examined CF-EPSCs of mice at P22-30 when CF innervation onto each PC has matured in normal mice (Hashimoto and Kano, 2003). CF-EPSCs were evoked by stimulating CFs in the granule cell layer. In both normal and *rkr* PCs, a large EPSC was elicited in an all-or-none fashion without contamination of PF-EPSCs as the stimulus intensity was gradually increased (Fig. 2A left). In some PCs, more than one discrete CF-EPSC could be elicited when the CF-stimulating electrode was moved systematically, and the stimulus intensity was increased gradually at each stimulation site, which reflected PCs innervated by multiple CFs (Fig. 2A right). I estimated the number of CFs innervating the PC by counting the number of discrete CF-EPSC steps. As shown in figure 2B, 83% (25 of 30 cells) and 77% (23 of 30 cells) of the PCs were innervated by single CFs in the normal and *rkr* mice, respectively, and the difference was not statistically significant ($p = 0.75$, Fisher's exact test). Furthermore, all the rest of the PCs showed two steps of CF-EPSCs, and more than three steps of the EPSCs were never found. Those indicated that developmental elimination of redundant CF

wiring was normal in *rkr* mice. Further analyses on CF-EPSCs were exclusively conducted in the PCs innervated by a single CF.

The current-voltage relationship for the peak current amplitude was linear (data not shown), and the reversal potential of them were statistically comparable (9.6 ± 0.6 mV ,n = 20 for normal mice; 11.1 ± 0.8 mV, n = 21 for *rkr* mice; $p = 0.16$), indicating the voltage-clamp conditions were comparable. The chord conductance of CF-EPSCs in *rkr* mice was significantly smaller than that of normal (Fig. 2C and Table 1; $p < 0.01$). To assess the kinetics of CF-EPSCs in *rkr* mice, I measured the 10-90% rise time and the decay time. Although, in *rkr* mice, the rise time was comparable to normal ($p = 0.14$), the decay time constant was significantly greater than normal (Fig. 2C and Table 1; $p < 0.001$). The paired-pulse depression magnitudes of CF-EPSCs in *rkr* mice were equivalent to normal at all pulse intervals tested (Fig 3C and D; 20 – 1000 ms).

In a native condition, CF activation generates strong depolarization named a complex spike in PCs (Llinás & Sugimori, 1980; Ito, 1984). To evaluate the influence of the changes of CF-EPSCs in a physiological condition, I examined the waveform of complex spikes in current-clamp mode. As shown figure 2D and E, CF stimulation could evoke complex spikes in *rkr* PCs, as well as normal PCs, and no significant change were observed in terms of spike number (normal, 3.0 ± 0.1, n = 19 cells; *rkr*, 3.5

± 0.25, n = 11 cells; p = 0.086), plateau potential (normal, 7.1 ± 0.6 mV, n = 13 cells; *rkr*, 7.4 ± 0.7 mV, n = 11 cells; p = 0.69), and after-hyperpolarization (normal, -1.8 ± 0.2 mV, n = 6 cells; *rkr*, -1.9 ± 0.1 mV, n = 6 cells; p = 0.80). These results suggested that CF inputs onto PCs in *rkr* mice were functionally normal.

Presynaptic function of the PF-PC synapses in rkr mice

In comparison of the synaptic properties in *rkr* mice with those in other $Ca_V2.1$ mutant mice thus far tested (Table 2; Matsushita et al., 2002; Miyazaki et al., 2004), I found that severe reduction of PF-EPSC amplitude were a prevalent phenotype, which suggested that function of the PF-PC synapses highly depended on the $Ca_V2.1$ channel function. To explore the origin of the severe reduction of PF-EPSCs in *rkr* mice, I first examined presynaptic properties of the PF-PC synapses, because the contribution of the $Ca_V2.1$ channel to the presynaptic Ca^{2+} influx that triggers neurotransmitter release is essential in the PF-PC synapses (Mintz et al., 1995). All experiments described below were carried out in mice at the age of 3-4 weeks (P22-34).

First, I applied a pair of stimulation pulses at different intervals and measured the paired-pulse facilitation (PPF) ratio of PF-EPSCs (the 2nd EPSC amplitude / the 1st EPSC amplitude, Fig. 3A, B). The PPF magnitude in *rkr* PCs was normal at all pulse

intervals tested (50-1000 ms, $p = 0.11$). Because PPF is considered to reflect the amount of residual Ca^{2+} in the presynaptic terminals (Zucker & Regehr, 2002), this finding suggested that the *rkr* mutation did not alter the Ca^{2+} influx much enough to change the PPF magnitude.

We next examined the sensitivity of PF-EPSCs to the extracellular Ca^{2+} concentration ($[Ca^{2+}]_e$). From this parameter, I can evaluate two factors; one is the degree of the saturation of the Ca^{2+} influx that is led by permeating Ca^{2+} ion binding to the pore of the channel, and the other is the supralinear relationship between the Ca^{2+} influx and the EPSC amplitude evoked (Mintz et al., 1995). As shown in figure 4A and B, the reduction of the $[Ca^{2+}]_e$ from 2 to 1 mM decreased the PF-EPSC amplitude to 31.2 ± 0.02% in *rkr* mice, which was similar to that in normal mice (29.6 ± 0.01%, $p = 0.51$). Elevating the $[Ca^{2+}]_e$ from 2 to 3 mM increased the PF-EPSC amplitude to 208.5 ± 0.07% in *rkr* mice, which was also comparable to that in normal mice (217.3 ± 0.09%, $p = 0.46$). We also assessed PPF ratio at 50 ms interval under the different $[Ca^{2+}]_e$ conditions, which revealed significant difference under 3 mM of $[Ca^{2+}]_e$ (1 mM of $[Ca^{2+}]_e$; 2.02 ± 0.07, n = 5 for normal mice; 1.83 ± 0.24, n = 3 for *rkr* mice; $p = 0.38$; 3 mM of $[Ca^{2+}]_e$; 1.52 ± 0.02, n = 5 for normal mice; 1.65 ± 0.03, n = 8 for *rkr* mice; $p < 0.01$). This elevation of PPF ratio in *rkr* mice implied a reduction of Ca^{2+} influx at the

PF terminals which might be so significant under an unphysiological condition that PPF ratio was changed. From these lines of evidence, we concluded that the sensitivity of PF-EPSCs to $[Ca^{2+}]_e$ was almost normal in *rkr* mice.

To further assess neurotransmitter release at the PF-PC synapses in *rkr* mice, I evaluated the glutamate concentration in the PF-PC synaptic clefts by using the low affinity AMPA receptor antagonist γ-DGG. This antagonist unbinds rapidly from AMPA receptors, and released glutamate will replace it at some binding sites. This feature allows me to use the degree of EPSC blockade by γ-DGG as an indicator of the glutamate concentration in the synaptic clefts (Liu et al., 1999; Wadiche & Jahr, 2001; Coesmans et al., 2004). 1 mM of γ-DGG reduced PF-EPSCs to 28.6 ± 0.01% for normal mice (n = 3), and 28.2 ± 0.02% for *rkr* mice (n = 5), and I could see no statistical difference between them (Fig. 4C, D, p = 0.88). This result indicated that, in the PF-PC synapses of *rkr* mice, the glutamate concentration in the synaptic cleft was comparable to normal. These lines of evidence indicated that the dysfunction of the presynaptic release machinery in *rkr* mice was, if any, quite modest, and unlikely to mainly account for the salient reduction of PF-PC synaptic transmission.

Postsynaptic alteration of the PF-PC synapses in rkr mice

Because the presynaptic functions were unexpectedly intact in the PF-PC synapses of *rkr* mice, I next examined the possibility that postsynaptic changes could account for the PF-EPSC reduction in *rkr* mice. Measurement of amplitude of miniature EPSCs is usually used for evaluation of the postsynaptic function. But electrophysiological evaluation of postsynaptic changes in the PF-PC synapses is difficult, because of the small unitary synaptic conductance and the noisy background current of PCs (see Discussion). To circumvent the problems, I directly counted the number of AMPA receptors by SDS-digested freeze-fracture replica labeling (SDS-FRL), which can reveal a two-dimensional structure of cell membranes and distribution of membrane proteins with high sensitivity (Fujimoto, 1995; Tanaka et al., 2005).

In the present study, I used SDS-FRL for samples from 3 normal mice and 3 *rkr* mice at P25-30, and carried out the same experiment twice on the samples. Both trials gave similar results, and I pooled them for statistical analyses. The primary antibody used in the present study reacted with a common extracellular epitope of AMPA receptor subunits GluR1-4 (Nusser et al., 1998; Tanaka et al., 2005), giving immunogold labeling for AMPA receptors on the E-face. To identify the PF-PC synapses on replicas, I sequentially labeled the glutamate receptor δ2 subunit (GluRδ2) with an antibody that

reacted with its extracellular epitope (Hirai, 2001) and gave immunogold labeling also on the E-face. GluRδ2 subunit is expressed exclusively in PCs, and localized selectively at the PF-PC synapses in the adult brain (Araki et al., 1993; Lomeli et al., 1993; Landsend et al., 1997), and is a good marker for the PF-PC synapses. Since excitatory synaptic areas are indicated by the IMP clusters on the E-face (Harris & Landis, 1986), I chose the IMP clusters that had more than one immunogold label for GluRδ2 within or nearby, and counted the number of immunogold particles within them. In view of the molecular size of an antibody, I accepted immunogold particles located within 10 nm from the boundary of the IMP clusters (Fig. 5).

The density of the immunogold particles for AMPA receptors in the PF-PC synaptic sites were 684.3 ± 444.2 particles/μm^2 for normal mice (mean ± SD, n = 300), and 453.2 ± 324.0 particles/μm^2 for *rkr* mice (mean ± SD, n = 284), revealing a significant reduction in *rkr* mice (~66% of normal; $p < 0.001$, Mann-Whitney U-test; Fig. 6A). The variance of the density of the labels was measured as coefficient of variance (SD/mean), and gave the comparable values (0.65 in normal mice; 0.71 in *rkr* mice). On the other hand, I also quantified the density of the immunogold particles for GluRδ2, which showed no significant change (mean ± SD; 100.7 ± 106.7 particles/μm^2, n = 300 for normal mice; 84.3 ± 66.3 particles/μm^2, n = 284 for *rkr* mice; $p = 0.11$, Mann-Whitney

U-test; Fig. 6B). Although I observed the immunogold particles for AMPA receptors out of IMP clusters, the density of them was much low and seemed comparable in normal and *rkr* mice.

The reduction of EPSCs, however, can be attributable not to the density of AMPA receptors, but to the total number of them per synapse. To evaluate the total number of AMPA receptors per synapse, I collected "complete synapses" that preserved whole of the synaptic IMP cluster on replicas from the whole data set (Fig. 7), and counted the number of the immunogold particles for AMPA receptors within them. The numbers of the particles for AMPA receptors were 27.8 ± 25.3 particles for normal mice (mean ± SD, n = 68), and 15.7 ± 15.9 particles for *rkr* mice (mean ± SD, n = 74), showing a significant reduction in *rkr* mice (~56% of normal; $p < 0.01$, Mann-Whitney U-test, Fig. 8A and D). In contrast, the numbers of the particles for GluRδ2 were not significantly changed (mean ± SD; 2.35 ± 1.46 particles, n = 68 for normal mice; 2.14 ± 1.96 particles, n = 74 for *rkr* mice; $p = 0.16$, Mann-Whitney U-test, Fig. 8B and E). I also measured the areas of the IMP clusters in the complete synapses, and found no significant difference (mean ± SD; 0.0358 ± 0.0239 μm^2, n = 68 in normal mice; 0.0349 ± 0.0201 μm^2, n = 74 in *rkr* mice; $p = 0.90$, Mann-Whitney U-test, Fig. 8C and F)

However, complete synapses on replicas may not represent whole population of the

PF-PC synapses, because freeze-fracture prefers structures with small curvature to be preserved on the fracture surface, and structures with large curvature like synapses on small spines are frequently broken. Therefore, I measured the synaptic area of the PF-PC synapses in normal and *rkr* mice by using electron microscopic reconstruction of the PF-PC synapses (Fig. 9A). In the reconstructed PF-PC synapses, the synaptic areas were 0.062 ± 0.030 μm^2 for normal mice (mean ± SD, n = 71 from 3 mice), and 0.058 ± 0.038 μm^2 for *rkr* mice (mean ± SD, n = 54 from 3 mice), showing no significant difference ($p = 0.23$, Mann-Whitney U-test, Fig. 9B and C). These lines of evidence indicated that the density of AMPA receptors was reduced, and the area of the synaptic sites was not changed in the PF-PC synapses of *rkr* mice, which resulted in the reduction of the total number of AMPA receptors per synapse. In contrast, the total number of GluRδ2 subunits remained normal.

Morphological alteration of the rkr Purkinje cells

Finally, I examined the possibility that the PF-EPSC reduction in *rkr* mice was partly attributable to the reduced number of the PF-PC synapses. I assessed the density of the PF-PC synapses in the upper molecular layer (ML), where I electrically elicited PF-EPSCs, by using the physical disector method on serial electron micrographs (Sterio,

1983; Coggeshall & Lekan, 1996). At P24-32, the density of the PF-PC synapses were 0.85 ± 0.17 / μm^3 for normal mice (mean ± SD, n = 122 of disectors from 3 mice, 532.5 μm^3 analyzed in total), and 0.93± 0.15 / μm^3 for *rkr* mice (mean ± SD, n = 120 of disectors from 3 mice, 483.0 μm^3 analyzed in total), indicating no significant difference ($p = 0.13$, Fig. 10D, E, and F). To examine the possibility that the number of PCs was altered, I also quantified the density of PCs by selectively staining PCs with anti-calbindin antibody and counting their somas with a confocal laser scanning microscope (CLSM) (Fig. 10A and B). At P22-29, the density of PCs were 3039 ± 569 / mm^2 for normal mice (mean ± SD, 33189 μm^2 of the PC layer analyzed in total from 3 mice), and 3185± 804 / mm^2 for *rkr* mice (mean ± SD, 43401 μm^2 of the PC layer analyzed in total from 3 mice), indicating no significant difference ($p = 0.58$, Fig. 10C). Thus I concluded that, in the upper ML, the average density of the PF-PC synapses per PC was normal in *rkr* mice, and did not account for the PF-EPSC reduction.

However, the branching pattern of PC dendrites could affect the amplitude of PF-EPSCs which are evoked by local stimulation in the ML; if PC dendrites are sparsely distributed in the ML, the number of the PF-PC synapses excited by stimulating local limitted area of the ML is decreased compared with the case where PC dendrites are densely distributed. Thus, I examined the morphology of PC dendrites in *rkr* mice at

P29-32 in detail. To visualize PCs for morphometric analysis, I injected biotinylated dextran amine into the cerebellar fastigial nucleus, and labeled PCs retrogradely (Sugihara et al., 1999). By this method, I could sparsely label and visualize PCs efficiently. After fluorescent staining, I carefully chose well-isolated PCs labeled without any truncation of dendrites from the straight portions of lobules 4, 5 and 6, and acquired image stacks containing the whole dendrites and soma by CLSM. To avoid any subjective bias, I collected all the PCs that fulfilled my criteria. The image stacks were converted into projection images to facilitate the morphometry, on which all further analyses were carried out.

As shown in figure 11A and B, I found that the dendrites of *rkr* PCs showed less arborization than those of normal PCs. The extent of branching complexity was evaluated by the number of crossings of the dendrites with evenly spaced lines that were parallel to the pia (Fig. 12A). The total number of crossings of the dendrites in *rkr* PCs was significantly less than that in normal PCs (mean ± SD; 480 ± 42.8 for normal mice; 394 ± 42.6 for *rkr* mice, $p < 0.001$). I found that the reduction was specifically severe in the region of the ML close to the pia where I electrically stimulated to evoke PF-EPSCs (Fig. 12B, $p < 0.05$ at 70%, $p < 0.001$ at 80 and 90% of ML level). To estimate the influence of the altered branching of PC dendrites on the amplitude of evoked

PF-EPSCs, I placed a semicircle so that its diameter faced the pia, and measured the total length of the dendrites contained within the semicircle. The semicircle was an assumed area where I electrically stimulated to evoke PF-EPSCs, and, as I placed the stimulus electrode, I located it where the total length of the dendrites within the semicircle reached the maximum (Fig. 12C). Since I could not see the precise size of the area electrically stimulated, I tried different diameters of the semicircle from 30 μm to 90 μm, which based on the size of the stimulus electrode (50 μm of diameter). As shown in Fig. 12D, the length of the dendrites contained within the semicircle was significantly reduced in *rkr* mice when the semicircles of 70 μm (mean ± SD; 719.5 ± 97.7 μm for normal mice, 580.2 ± 99.3 μm for *rkr* mice, $p < 0.01$) and 90 μm of diameters (mean ± SD; 1132.4 ± 181.0 μm for normal mice, 890.8 ± 167.6 μm for *rkr* mice, $p < 0.001$) were tested. I further examined whether the density of the PF-PC synapses along a PC dendrite was altered in *rkr* mice. Counting the number of the spines on distal PC dendrites in the subpial region, I found that there was no significant difference between normal and *rkr* mice (2.18 ± 0.06 / μm, 274.7 μm analyzed in normal mice; 2.24 ± 0.05 / μm, 274.1 μm analyzed in *rkr* mice; $p = 0.54$; Fig. 12E and F). We also found that the percentage of the PF-PC synapses with multiple contact between PF terminals and PC spines (Rhyu et al., 1999a and 1999b; Miyazaki et al.,

2004) was not significantly different between normal and *rkr* mice(Fig. 5; 1.66 ± 0.69% in normal mice, n = 3, 1998.25 μm^2 analyzed in total; 2.36 ± 2.40% in *rkr* mice, n = 3, 1973.71 μm^2 analyzed in total; $p = 0.65$)

These lines of evidence indicated that, even at younger age, the dendrites of PCs showed the abnormal arborization in *rkr* mice, and suggested that the altered branching of PC dendrites may partly account for the reduction of PF-EPSCs. The total length of PC dendrites was also significantly reduced in *rkr* mice (mean ± SD; 5464.0 ± 462.6 μm for normal mice, 4064.7 ± 492.0 μm for *rkr* mice, $p < 0.001$), which would partly reflect the shrinking of the ML (The thickness of the ML of the lobule 4 and 5, mean ± SD; 164.5 ± 17.9 μm for normal mice, 140.0 ± 14.5 μm for *rkr* mice, $p < 0.001$), and suggested that the total number of the PF-PC synapses per PC was also reduced in *rkr* PCs.

Discussion

The presented results demonstrated that the dysfunction of the $Ca_V2.1$ channel suffering *rkr* mutation resulted in a severe impairment of synaptic transmission in the PF-PC synapses in *rkr* mice, reducing the amplitude of PF-EPSC to 31% of normal. On the other hand, CF-EPSCs in *rkr* mice showed limited changes on their properties including a reduction of conductance to 66% of normal and a slower current decay, which had no significant effect on the generation of complex spikes. I revealed that the synaptic impairment involved a reduction of postsynaptic AMPA receptors, whereas I could not find any changes in the presynaptic function and the density of the PF-PC synapses per PC in the ML. I also observed an abnormal arborization of PC dendrites in *rkr* mice at one month of age, which may partly account for the reduction of the PF-EPSC amplitude. To understand physiological processes where the $Ca_V2.1$ channel plays a major role and $Ca_V2.1$ mutations have an impact, I further discuss the characteristics of the *rkr* phenotypes especially in the context of comparative analyses with other $Ca_V2.1$ mutant mice including *tottering, leaner, rolling*, and $Ca_V2.1$ knockout (KO) mice, and consider the pathogenetic mechanism underlying the phenotypes.

Impaired transmission of the PF-PC synapses in rkr mice.

In spite of the moderate change of the *rkr* mutant channel function, synaptic transmission in the PF-PC synapses was severely impaired in *rkr* mice. A similar phenotype was reported in *tottering* and *rolling* mice (Matsushita et al., 2002), and my result supports the notion that the function of the PF-PC synapses highly depends on the $Ca_V2.1$ channel. At the 3-4 weeks of age, the amplitude of PF-EPSCs was reduced to a comparable level in *rkr* (31%) and *tottering* mice (28%) (*Rolling* mice were tested only at P14-20).

In exploring the origin of the reduction of the PF-PC synaptic transmission, I first electrophysiologically analyzed transmitter release in the PF-PC synapses where the $Ca_V2.1$ channel dominantly mediates presynaptic Ca^{2+} influx (Mintz et al., 1995). Contrary to my expectation, presynaptic function in the *rkr* PF-PC synapses showed the normal properties in terms of paired-pulse facilitation and sensitivity to $[Ca^{2+}]_e$, suggesting a normal Ca^{2+} dynamics and a normal release probability at the release sites. Moreover, the blocking effect of γ-DGG did not show a significant difference between normal and *rkr* mice, indicating a normal glutamate concentration in the PF-PC synaptic clefts in *rkr* mice. These lines of evidence suggested that the transmission impairment in the *rkr* PF-PC synapses could not be attributable to presynaptic dysfunction. The normal

kinetics of PF-EPSCs in *rkr* mice supports the intact presynaptic function.

The normal presynaptic function in the *rkr* PF-PC synapses would be explained by the compensation mechanism for the mutant $Ca_V2.1$ channel by other types of VDCCs. It was shown that the dependence on $Ca_V2.2$ (N-type) and presumed $Ca_V2.3$ (R-type) channels was augmented in the PF-PC synapses of *tottering* and *rolling* mice (Matsushita et al., 2002), and in hippocampal synapses, the dependence on $Ca_V2.2$ was enhanced in *tottering* (Qian & Noebels, 2000) and $Ca_V2.1$ KO mice (Jun et al., 1999). Therefore, it is likely that $Ca_V2.1$ dysfunction in presynapses of the *rkr* PF-PC synapses is compensated by upregulation of other Ca^{2+} channel subtypes.

We then examined the possibility of postsynaptic alteration in the *rkr* PF-PC synapses. In pilot experiments (data not shown), I found that it was very difficult to record miniature EPSCs or unitary EPSCs in PCs from mice older than 3 weeks, because there was a great amount of baseline noise, which made it impossible to identify miniature EPSCs or unitary EPSCs with certainty (Takahashi & Linden, 2000). The noise was resistant to fast synaptic transmission blockers (10 μM CNQX and 10 μM bicuculline), voltage-dependent channel blockers (1 μM TTX, 100 μM $CdCl_2$, and 60 mM CsCl and 20 mM TEA in pipette solution), and a Ca^{2+} chelator (20 mM BAPTA in pipette solution). I presume that the noise reflects currents emerged from unclamped regions of

distal dendrites. I also tried to measure currents elicited by direct application of AMPA to PC dendrites. However, the amplitudes of the currents were highly variable and unsuitable for quantitative comparison among cells or animals.

Then, I directly evaluated the number of AMPA receptors by SDS-FRL, which enables me to quantify the number of membrane proteins including AMPA receptors with high sensitivity (Tanaka et al., 2005). Using SDS-FRL, I revealed that the number of postsynaptic AMPA receptors per PF-PC synapse was reduced to 66% of normal, whereas that of GluRδ2 remained normal. It indicates that a fairly moderate dysfunction of the $Ca_V2.1$ channel can affect the synaptic content of AMPA receptors, and demonstrates the roll of the $Ca_V2.1$ channel in determining the number of postsynaptic AMPA receptors in the PF-PC synapses. The number of AMPA receptors is also well known as one of the central substrates of synaptic plasticity (Song & Huganir, 2002). In SDS-FRL, the variance of the density of immunogold particles for AMPA receptors that is supposed to reflect synaptic plasticity, remained comparable to normal in *rkr* mice, suggesting that a substantial disruption of synaptic plasticity is unlikely.

One possible pathogenetic mechanism causing the AMPA receptor reduction is the reduction of Ca^{2+} influx in *rkr* PCs. The $Ca_V2.1$ channel predominantly mediates Ca^{2+} influx in PCs, because PCs is devoid of NMDA receptors and Ca^{2+} permeable AMPA

receptors in adult animals (Hartmann & Konnerth, 2005). A recent report demonstrated that the local intracellular Ca^{2+} level could regulate the lateral movement of AMPA receptors in cultured hippocampal neurons, suggesting a roll of the Ca^{2+} influx in establishment of novel synapses (Borgdorff & Choquet, 2002). Thus even the small reduction of Ca^{2+} influx in *rkr* PCs may indirectly induce the reduction of AMPA receptors. In acutely dissociated PC somas, the reduction of the Ca^{2+} current density in *rkr* mice was estimated to 77% of normal (Itsukaichi et al., 2002). However, it is likely that the absolute amount of Ca^{2+} entry in dendrites, especially in spines, is more severely decreased, because the $Ca_V2.1$ channel densely localized on them (Kulik et al., 2004). Thus, the mild dysfunction of the $Ca_V2.1$ channel may cause a substantial change of intracellular Ca^{2+} level in PC spines, which can result in an abnormal synaptic composition including reduced number of AMPA receptors.

Another possibility is the impaired association of the $Ca_V2.1$ channel with postsynaptic components including AMPA receptors. Resent studies indicate a functional association of the $Ca_V2.1$ channel with AMPA receptors, PSD95 (Kang et al., 2006) and transmembrane AMPA receptor regulatory proteins (TARPs; Rousset et al., 2001; Kang et al., 2001), a protein family having some homology to a Ca^{2+} channel subunit γ1, and playing an essential roll in the control of both AMPA receptor trafficking and its gating

(Nicoll et al., 2006). Therefore, the *rkr* mutation may disrupt direct interaction between the $Ca_V2.1$ channel and AMPA receptor or its modulatory proteins, which may impair maintaining the normal number of AMPA receptors in the postsynaptic sites. It is also possible that, in *rkr* PCs, the number of functional complexes containing the $Ca_V2.1$ channel is insufficient to maintain normal postsynaptic organization, because, as inferred from the reduction of the Ca^{2+} channel current density, the expression level of the $Ca_V2.1$ channel may be decreased.

The altered properties of CF-PC synapses in rkr mice

The CF-PC synapses in *rkr* mice showed a substantial reduction of chord conductance to 66% of normal, and slower decay of the EPSCs. The reduction of the chord conductance is remarkable because those in the *tottering*, *rolling Nagoya*, and $Ca_V2.1$ KO mice are normal or rather increased (Matsushita et al., 2002; Miyazaki et al., 2004). Although I do not have a proper explanation for this divergence for now, it may reflect the complexity of the rolls the $Ca_V2.1$ channel takes a part in to form and consolidate CF-PC synapses. The slower decay of CF-EPSCs also reported in *rolling* and $Ca_V2.1$ KO mice, which seemed to be attributable to an altered property of postsynaptic AMPA receptors (Matsushita et al., 2002).

The CF inputs in vivo evoke complex spikes in PCs: a large depolarization, spike generation, and following elevation of intracellular Ca^{2+} level, which is a requisite for the modulations of synaptic response including long-term depression of PF-PC synaptic transmission (Ito, 2001). I analyzed the waveform of complex spikes in *rkr* mice and found it normal, suggesting that the functional impact of the changes in CF-EPSCs in *rkr* mice is, if any, small. Moreover, multiple innervation of CFs onto PCs is as minor in *rkr* mice as in normal mice. These lines of evidence suggested that, when compared with the PF-PC synapses, the CF-PC synapses are functionally tolerant to the $Ca_V2.1$ dysfunction.

Abnormal morphology of rkr *PCs*

In *rkr* mice of more than one year of age, PC dendrites exhibit a characteristic "weeping willow" appearance in which the ends of the secondary branches appear to extend, often turning and growing back toward the soma (Zwingman et al., 2001). I did not observe such a striking morphological change in *rkr* PCs at P29-32. However, using CSLM observation of PCs labeled by BDA, I revealed a mild but significant branching abnormality of dendrites especially in the upper ML of *rkr* mice, which resulted in the reduced content of PC dendrites per area (~80% of normal), and may partly account for

the reduced amplitude of PF-EPSCs. Since I observed the normal density of the PF-PC synapses per PC in the upper ML of *rkr* mice, the reduced content of PC dendrites suggested that, in *rkr* mice, overall content of PC dendrites in the upper ML was not changed, but the distribution of the dendrites belonging to each PC was rather inhomogeneous, which resulted in a deformed territory of PC dendrites in the ML (Fig. 11). I confirmed that the planarity of PC dendrites was preserved in *rkr* mice (data not shown). Thus the change of dendritic arborization in *rkr* PCs was restricted in the plane of PC dendrites.

There have been a number of reports about the determinants of the PC dendrite arborization including bioelectrical activity of PCs, afferent inputs, hormones, neurotrophins, and activity of protein kinase C (for review, see Kapfhammer, 2004). Among them, afferent inputs mainly from parallel fibers are especially required for high-order branching. Thus the impaired transmission of the PF-PC synapses in *rkr* mice may be involved in the abnormal dendritic branching. As Zwingman et al (2001) has shown, the shape of PC dendrites I observed in *rkr* mice at one month of age is dramatically transformed into the “weeping willow” appearance in a later lifetime of animals. Although there are some reports about the morphological change of PC dendrites during a lifetime of animal (Weiss & Pysh, 1978; Sadler & Berry, 1984),

underlying mechanisms of it remain unclear. Further studies on $Ca_V2.1$ mutants may give a clue to understand the maintenance and remodeling of the dendritic arborization in PCs of adult animals.

Unrevealed synaptic components impairing the PF-PC synaptic transmission in rkr mice

As mentioned above, I revealed the reduction of postsynaptic AMPA receptors in the PF-PC synapses (~66% of normal), and the reduced content of PC dendrites per area of the upper ML (~80% of normal) in *rkr* mice, both of which can account for the reduced amplitude of PF-EPSCs (~31%). However, there may be other changes involved in the impaired transmission of the PF-PC synapses in *rkr* mice. A candidate is a change in a property of postsynaptic AMPA receptors. Altered sensitivity of AMPA receptors to AMPA was observed in *rolling* mice (Matsushita et al., 2002), which suggested the $Ca_V2.1$ dysfunction could change a property of AMPA receptors. It is known that the functional properties of AMPA receptors can be modified by phosphorylation (Gomes et al., 2003). Some kinases and phosphatases (e.g., Ca^{2+} / calmodulin-dependent protein kinase II, calcineurin) are controlled by intracellular Ca^{2+} level, activities of which may be affected by the *rkr* mutation. Moreover, because Intracellular Ca^{2+} level can modify

the pattern of the gene expression, the *rkr* mutaion may result in different composition of AMPA receptor subunits. Further studies are expected to elucidate impact of the $Ca_V2.1$ dysfunction on Ca^{2+}-dependent molecular metabolism in the intracellular environment.

Future direction

To understand the pathogenetic mechanism in $Ca_V2.1$ mutant mice, it is essential to characterize the neurological symptoms (e.g., ataxia) as an abnormal firing pattern of relevant neuronal population. For this aim, I am attempting to evaluate in vivo activity of cerebellar neurons in *rkr* mice. As shown Fig. 13A and B, I extracellularly recorded unit firings of PCs under anesthesia with urethane. It was thus far consistently observed that regularity of spontaneous firing of simple spikes was severely impaired in *rkr* mice, which was apparent in comparison of autocorrelograms from normal and *rkr* mice (Fig. 13C and D). A similar abnormality has been reported in *tottering* mice (Hoebeek et al., 2005). I am also trying to evaluate the response of PCs to an external natural stimulation (Fig. 13E). In response to an air puff on the perioral skin, some PCs in simplex lobule, crus I, and crus II showed a decreased discharge rate of simple spikes, whereas that of complex spikes was augmented (Fig. 13F). I hope that, by studying on this relatively simple system, basic characters of abnormal neural activities in $Ca_V2.1$ mutant mice will be revealed, and understood in relationship with the synaptic dysfunctions thus far I have reported. I also expect that these studies will propose us a new treatment strategy of human disorders caused by $Ca_V2.1$ mutations including episodic ataxia type 2 (Ophoff et al., 1996) and spinocerebellar ataxia type 6 (Zhuchenko et al., 1997).

References

Araki, K., Meguro, H., Kushiya, E., Takayama, C., Inoue, Y. & Mishina, M. (1993) Selective expression of the glutamate receptor channel δ2 subunit in cerebellar Purkinje cells. *Biochem. Biophys. Res. Commun.*, **197**, 1267-1276.

Borgdorff, A. J. & Choquet, D. (2002) Regulation of AMPA receptor lateral movements. *Nature*, **417**, 649-653.

Catterall, W. A. (1998) Structure and function of neuronal Ca^{2+} channels and their role in neurotransmitter release. *Cell Calcium*, **24**, 307-323.

Coesmans, M., Weber, J. T., De Zeeuw, C. I. & Hansel, C. (2004) Bidirectional parallel fiber plasticity in the cerebellum under climbing fiber control. *Neuron*, **44**, 691-700.

Coggeshall, R. E. & Lekan, H. A. (1996) Methods for determining numbers of cells and synapses: a case for more uniform standards of review. *J. Comp. Neurol.*, **364**, 6-15.

Ertel, E. A., Campbell, K. P., Harpold, M. M., Hofmann, F., Mori, Y., Perez-Reyes, E., Schwartz, A., Snutch, T. P., Tanabe, T., Birnbaumer, L., Tsien, R. W. & Catterall, W. A. (2000) Nomenclature of voltage-gated calcium channels. *Neuron*, **25**, 533-535.

Fujimoto, K. (1995) Freeze-fracture replica electron microscopy combined with SDS digestion for cytochemical labeling of integral membrane proteins. Application to the immunogold labeling of intercellular junctional complexes. *J. Cell Sci.*, **108 (Pt 11)**, 3443-3449.

Gomes, A. R., Correia, S. S., Carvalho, A. L. & Duarte, C. B. (2003) Regulation of AMPA receptor activity, synaptic targeting and recycling: role in synaptic plasticity. *Neurochem. Res.*, **28**, 1459-1473.

Harris, K. M. & Landis, D. M. D. (1986) Membrane structure at synaptic junctions in area CA1 of the rat hippocampus. *Neuroscience*, **19**, 857-872.

Hartmann, J. & Konnerth, A. (2005) Determinants of postsynaptic Ca^{2+} signaling in Purkinje neurons. *Cell Calcium*, **37**, 459-466.

Hashimoto, K., and Kano, M. (2003) Functional differentiation of multiple climbing fiber inputs during synapse elimination in the developing cerebellum. *Neuron*, **38**, 785-796.

Hirai, H. (2001) Ca^{2+}-dependent regulation of synaptic δ2 glutamate receptor density in cultured rat Purkinje neurons. *Eur. J. Neurosci.*, **14**, 73-82.

Hoebeek, F. E., Stahl, J. S., van Alphen, A. M., Schonewille, M., Luo, C., Rutteman, M., van den Maagdenberg, A. M. J. M., Molenaar, P. C., Goossens, H. H. L. M., Frens, M. A., and De Zeeuw, C. I. (2005) Increased noise level of Purkinje cell activities minimizes impact of their modulation during sensorimotor control. *Neuron*, **45**, 953-965.

Itsukaichi, Y., Mori, E., Imoto, K., Tsubokawa, H., Zwingman, T., Herrup, K., Oka, H. & Mori, Y. (2002) Rocker mutation alters P/Q-type calcium channel properties in cerebellar Purkinje cells and the recombinant expression system. *Soc. Neurosci. Abstr.* **28**, 251.258.

Ino, M., Yoshinaga, T., Wakamori, M., Miyamoto, N., Takahashi, E., Sonoda, J., Kagaya, T., Oki, T., Nagasu, T., Nishizawa, Y., Tanaka, I., Imoto, K., Aizawa, S., Koch, S., Schwartz, A., Niidome, T., Sawada, K., Mori, Y. (2001) Functional disorders of the sympathetic nervous system in mice lacking the α_{1B} subunit ($Ca_V2.2$) of N-type calcium channels. *Proc. Natl. Acad. Sci. USA*, 98, 5323-5328.

Ito, M. (1984) *The cerebellum and neural control*. Raven Press, New York.

Ito, M. (2001) Cerebellar long-term depression: characterization, signal transduction, and functional roles. *Physiol. Rev.*, **81**, 1143-1195.

Jun, K., Piedras-Renteria, E. S., Smith, S. M., Wheeler, D. B., Lee, S. B., Lee, T. G., Chin, H., Adams, M. E., Scheller, R. H., Tsien, R. W. & Shin, H. S. (1999) Ablation of P/Q-type Ca^{2+} channel currents, altered synaptic transmission, and progressive ataxia in mice lacking the α_{1A}-subunit. *Proc. Natl. Acad. Sci. USA*, **96**, 15245-15250.

Kang, M. G., Chen, C. C., Felix, R., Letts, V. A., Frankel, W. N., Mori, Y. & Campbell,

K. P. (2001) Biochemical and biophysical evidence for γ_2 subunit association with neuronal voltage-activated Ca^{2+} channels. *J. Biol. Chem.*, **276**, 32917-32924.

Kang, M. G., Chen, C. C., Wakamori, M., Hara, Y., Mori, Y. & Campbell, K. P. (2006) A functional AMPA receptor-calcium channel complex in the postsynaptic membrane. *Proc. Natl. Acad. Sci. USA*, **103**, 5561-5566.

Kapfhammer, J. P. (2004) Cellular and molecular control of dendritic growth and development of cerebellar Purkinje cells. *Prog. Histochem. Cytochem.*, **39**, 131-182.

Kulik, Á., Nakadate, K., Hagiwara, A., Fukazawa, Y., Luján, R., Saito, H., Suzuki, N., Futatsugi, A., Mikoshiba, K., Frotscher, M. & Shigemoto, R. (2004) Immunocytochemical localization of the α_{1A} subunit of the P/Q-type calcium channel in the rat cerebellum. *Eur. J. Neurosci.*, **19**, 2169-2178.

Landsend, A. S., Amiry-Moghaddam, M., Matsubara, A., Bergersen, L., Usami, S., Wenthold, R. J. & Ottersen, O. P. (1997) Differential localization of δ glutamate receptors in the rat cerebellum: coexpression with AMPA receptors in parallel fiber-spine synapses and absence from climbing fiber-spine synapses. *J. Neurosci.*, **17**, 834-842.

Llinás, R., and Sugimori, M. (1980) Electrophysiological properties of *in vitro* Purkinje cell somata in mammalian cerebellar slices. *J. Physiol.*, **305**, 171-195.

Liu, G., Choi, S. & Tsien, R. W. (1999) Variability of neurotransmitter concentration and nonsaturation of postsynaptic AMPA receptors at synapses in hippocampal cultures and slices. *Neuron*, **22**, 395-409.

Lomeli, H., Sprengel, R., Laurie, D. J., Köhr, G., Herb, A., Seeburg, P. H. & Wisden, W. (1993) The rat delta-1 and delta-2 subunits extend the excitatory amino acid receptor family. *FEBS Lett.*, **315**, 318-322.

Matsushita, K., Wakamori, M., Rhyu, I. J., Arii, T., Oda, S., Mori, Y. & Imoto, K. (2002) Bidirectional alterations in cerebellar synaptic transmission of *tottering* and *rolling* Ca^{2+} channel mutant mice. *J. Neurosci.*, **22**, 4388-4398.

Meijering, E., Jacob, M., Sarria, J. C. F., Steiner, P., Hirling, H. & Unser, M. (2004) Design and validation of a tool for neurite tracing and analysis in fluorescence microscopy images. *Cytometry*, **58A**, 167-176.

Mintz, I. M., Sabatini, B. L. & Regehr, W. G. (1995) Calcium control of transmitter release at a cerebellar synapse. *Neuron*, **15**, 675-688.

Miyazaki, T., Hashimoto, K., Shin, H. S., Kano, M., and Watanabe, M. (2004) P/Q-type Ca^{2+} channel α_{1A} regulates synaptic competition on developing cerebellar Purkinje cells. *J. Neurosci.*, **24**, 1734-1743.

Nicoll, R. A., Tomita, S. & Bredt, D. S. (2006) Auxiliary subunits assist AMPA-type glutamate receptors. *Science*, **311**, 1253-1256.

Nusser, Z., Lujan, R., Laube, G., Roberts, J. D., Molnar, E. & Somogyi, P. (1998) Cell type and pathway dependence of synaptic AMPA receptor number and variability in the hippocampus. *Neuron*, **21**, 545-559.

Ophoff, R. A., Terwindt, G. M., Vergouwe, M. N., van Eijk, R., Oefner, P. J., Hoffman, S. M. G., Lamerdin, J. E., Mohrenweiser, H. W., Bulman, D. E., Ferrari, M., Haan, J., Lindhout, D., van Ommen, G. J. B., Hofker, M. H., Ferrari, M. D., and Frants, R. R. (1996) Familial hemiplegic migraine and episodic ataxia type-2 are caused by mutations in the Ca^{2+} channel gene CACNL1A4. *Cell*, **87**, 543-552.

Qian, J. & Noebels, J. L. (2000) Presynaptic Ca^{2+} influx at a mouse central synapse with Ca^{2+} channel subunit mutaions. *J. Neurosci.*, **20**, 163-170

Regehr, W. G., and Mintz, I. M. (1994) Participation of multiple calcium channel types in transmission at single climbing fiber to Purkinje cell synapses. *Neuron*, **12**, 605-613.

Rhyu, I. J., Abbott, L. C., Walker, D. B. & Sotelo C. (1999) An ultrastructural study of granule cell/Purkinje cell synapses in tottering (*tg*/*tg*), leaner (tg^{la}/tg^{la}) and compound heterozygous tottering/leaner (tg/tg^{la}) mice. *Neuroscience*, **90**, 717-728.

Rhyu, I. J., Oda, S., Uhm, C. S., Kim, H., Suh, Y. S. & Abbott, L. C. (1999) Morphological investigation of *rolling* mouse Nagoya (tg^{rol}/tg^{rol}) cerebellar Purkinje

cells: an ataxic mutant, revisited. *Neurosci. lett.* **266**, 49-52.

Rousset, M., Cens, T., Restituito, S., Barrere, C., Black, J. L., III, McEnery, M. W. & Charnet, P. (2001) Functional roles of γ_2, γ_3 and γ_4, three new Ca^{2+} channel subunits, in P/Q-type Ca^{2+} channel expressed in *Xenopus* oocytes. *J. Physiol.*, **532**, 583-593.

Sadler, M. & Berry, M. (1984) Remodelling during development of the Purkinje cell dendritic tree in the mouse. *Proc. R.. Soc. Lond.B. Bio. Sci.*, **221**, 349-368.

Schneggenburger, R. & Neher, E. (2005) Presynaptic calcium and control of vesicle fusion. *Curr. Opin. Neurobiol.*, **15**, 266-274.

Sochivko, D., Pereverzev, A., Smyth, N., Gissel, C., Schneider, T.& Beck, H. (2002) The $Ca_V2.3$ Ca^{2+} channel subunit contributes to R-type Ca^{2+} currents in murine hippocampal and neocortical neurons. *J. Physiol.*, 542, 699-710

Song, I. & Huganir, R. L. (2002) Regulation of AMPA receptors during synaptic plasticity. *Trends Neurosci.*, **25**, 578-588.

Stahl, J. S. (2004) Eye movements of the murine P/Q calcium channel mutant *rocker*, and the impact of aging. *J. Neurophysiol.*, **91**, 2066-2078.

Stahl, J. S. & James, R. A. (2005) Neural Integrator Function in Murine CACNA1A Mutants. *Ann. N.Y. Acad. Sci.*, **1039**, 580-582.

Sterio, D. C. (1984) The unbiased estimation of number and sizes of arbitrary particles using the disector. *J. Microsc.,* **134 (Pt 2)**, 127-136.

Sugihara, I., Wu, H. S. & Shinoda, Y. (1999) Morphology of single olivocerebellar axons labeled with biotinylated dextran amine in the rat. *J. Comp. Neurol.*, **414**, 131-148.

Takahashi, K. A., and Linden, D. J. (2000) Cannabinoid receptor modulation of synapses received by cerebellar Purkinje cells. *J. Neurophysiol.*, **83**, 1167-1180.

Tanaka, J., Matsuzaki, M., Tarusawa, E., Momiyama, A., Molnar, E., Kasai, H. &

Shigemoto, R. (2005) Number and density of AMPA receptors in single synapses in immature cerebellum. *J. Neurosci.*, **25**, 799-807.

Weiss, G. M. & Pysh, J. J. (1978) Evidence for loss of Purkinje cell dendrites during late development: A morphometric Golgi analysis in the mouse. *Brain Res.*, **154**, 219-230.

Wadiche, J. I. & Jahr, C. E. (2001) Multivesicular release at climbing fiber-Purkinje cell synapses. *Neuron*, **32**, 301-313.

Zhuchenko, O., Bailey, J., Bonnen, P., Ashizawa, T., Stockton, D. W., Amos, C., Dobyns, W. B., Subramony, S. H., Zoghbi, H. Y., and Lee, C. C. (1997) Autosomal dominant cerebellar ataxia (SCA6) associated with small polyglutamine expansions in the α_{1A} -voltage-dependent calcium channel. *Nat. Genet.*, **15**, 62-69.

Zucker, R. S. & Regehr, W. G. (2002) Short-term synaptic plasticity. *Annu. Rev. Physiol.*, **64**, 355-405.

Zwingman, T. A., Neumann, P. E., Noebels, J. L. & Herrup, K. (2001) Rocker is a new variant of the voltage-dependent calcium channel gene *Cacna1a*. *J. Neurosci.*, **21**, 1169-1178.

Acknowledgements

I am deeply grateful to Drs. Keiji Imoto, Mariko Miyata, Shin'ichiro Satake, and Tsuyoshi Inoue, for their generous supports and valuable guidance through this study, Drs. Ryuichi Shigemoto and Yugo Fukazawa for instructing electron microscopic analyses including SDS-FRL, and Drs. Elek Molnar and Miwako Masugi-Tokita for providing antibodies. I would like to thank Mrs. Naomi Fukuta, Sachiko Yamada, Sanae Hara, and Hiromi Nomura for their excellent technical assistance. I wish to thank all the members of Division of Neural Signaling for their supports, kindness and inspiring discussion.

Figures and tables

Figure 1.

PF-PC transmission in *rkr* mice. (A and B) Representative traces of PF-EPSCs from normal and *rkr* PCs at P13-15 (A) or at P23-26 (B). The EPSCs evoked by the stimuli with the series of intensity (from 5 to 20 μA with 2.5 μA step) are overlaid. (C and D) Mean peak amplitudes of PF-EPSCs are plotted as a function of the stimulus intensity for normal (blue open circles, n = 10) and *rkr* (red filled circles, n = 11) mice at P13-15 (C) or at P23-26 (D). Statistical significance was tested by repeated ANOVA followed by Bonferroni test. All error bars represent SEM. *p<0.05; **p<0.01; ***,p<0.001.

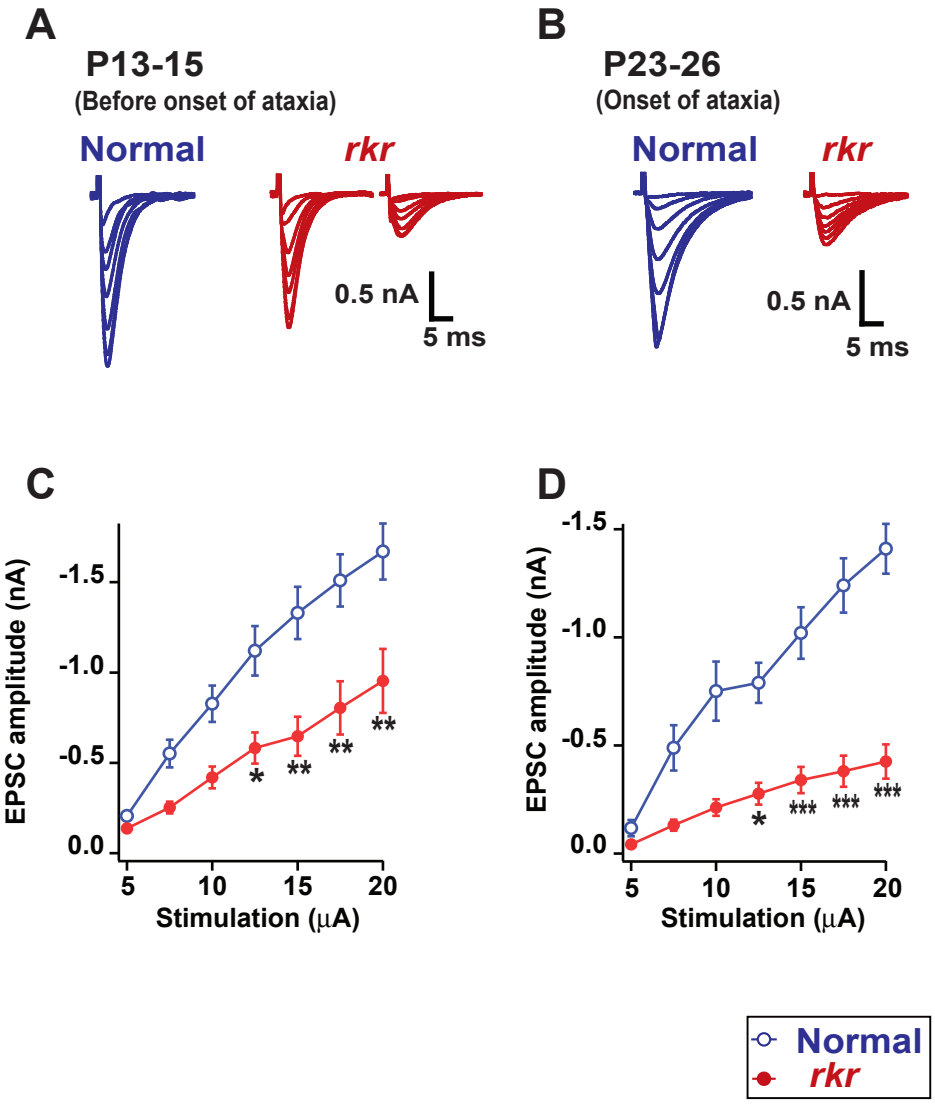
A
P13-15
(Before onset of ataxia)
Normal
rkr
0.5 nA
5 ms
B
P23-26
(Onset of ataxia)
Normal
rkr
0.5 nA
5 ms
C
EPSC amplitude (nA)
-1.5
-1.0
-0.5
0.0
5
10
15
20
Stimulation (μA)
*
**
**
**
D
EPSC amplitude (nA)
-1.5
-1.0
-0.5
0.0
5
10
15
20
Stimulation (μA)
*
***
***
***
Normal
rkr

Fig. 1

Figure 2.

CF-PC transmission in *rkr* mice. (A) Representative traces of CF-EPSCs demonstrating multiple CF innervation of PCs. Two to three traces are overlaid at each threshold stimulus intensity. Holding potential was 0 mV. Left traces show one step of CF-EPSC, while right traces show two steps of CF-EPSC. I systematically moved stimulus electrode in granule cell layer to obtain the maximum number of step of CF-EPSCs that corresponded to the number of CFs innervating the PC. Both traces were obtained from a *rkr* mouse at P27-29. Stimulus artifacts are removed for clarity. (B) Summary histograms showing the number of discrete steps pf CF-EPSCs from the normal (blue open columns; n = 30 PCs, 2 mice) and *rkr* mice (red filled column; n = 30 PCs, 2 mice). (C) Representative traces of CF-EPSCs at –10 mV of driving force from normal (left) and *rkr* (middle) PCs at P22-30. Stimulus artifacts are removed by subtracting the trace obtained at reversal potential. The traces normalized to the peak of the EPSC are overlaid (right, blue trace for normal, red trace for *rkr*). (D and E) Waveform of complex spikes in *rkr* mice. Representative traces of complex spikes in normal (D and E, left) and *rkr* (D and E, right) PCs are shown. The spikes and the following plateau potential are shown in (D). The After-hyperpolarization at a slower sweep speed are shown in (E). Dotted line indicates the resting potential. The initial portions of evoked

response are truncated by expansion in (E).

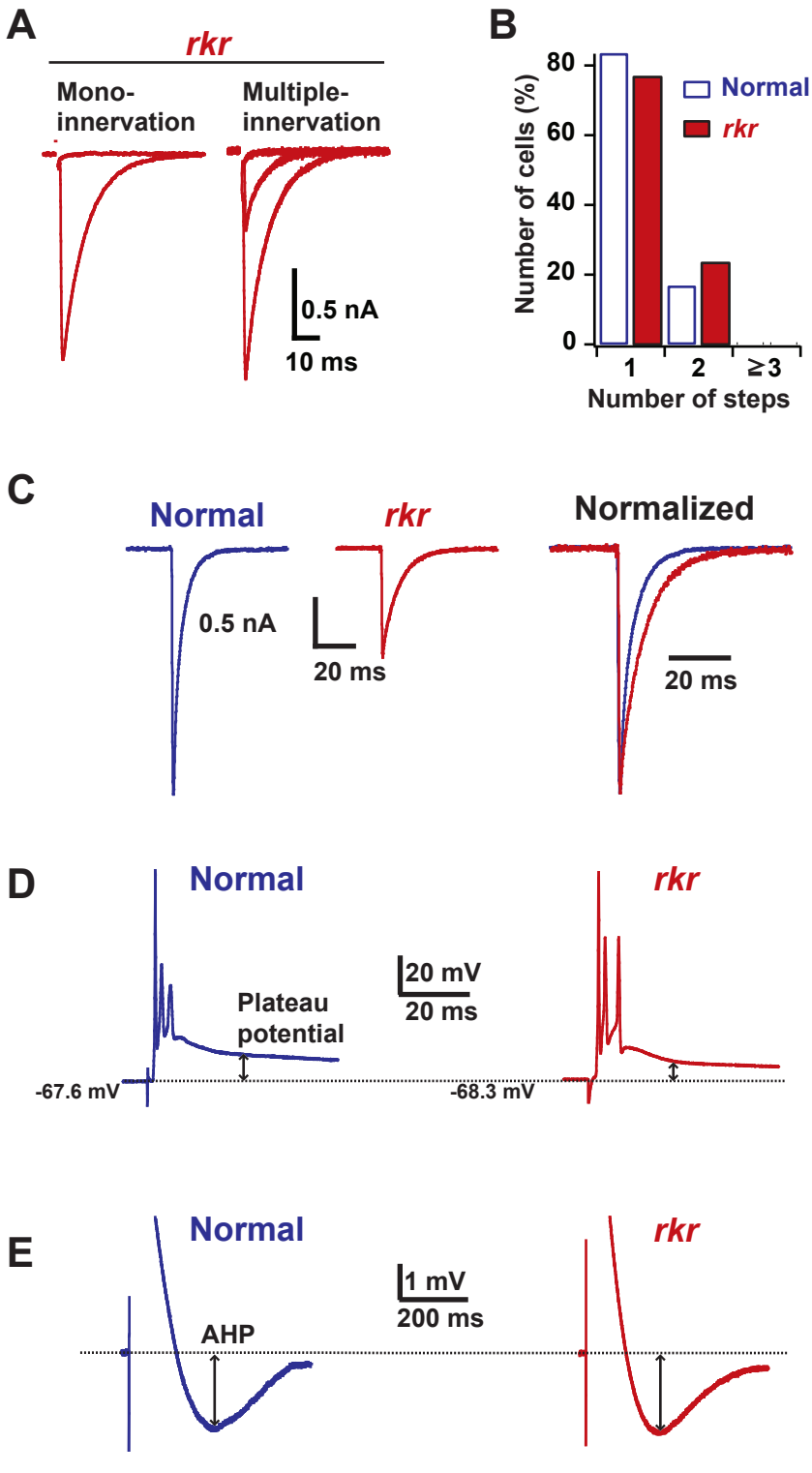
A
rkr
Mono-
innervation
Multiple-
innervation
0.5 nA
10 ms
B
Number of cells (%)
80
60
40
20
0
Normal
rkr
1
2
≥3
Number of steps
C
Normal
rkr
Normalized
0.5 nA
20 ms
20 ms
D
Normal
rkr
Plateau
potential
20 mV
20 ms
-67.6 mV
-68.3 mV
E
Normal
rkr
1 mV
200 ms
AHP

Fig. 2

Figure 3.

EPSCs evoked by the paired-pulse stimulation. (A) Representative traces of PF-EPSCs evoked by the paired-pulse stimulation (50 ms interval). Traces are normalized to the peaks of the first EPSC (right, blue trace for normal, red trace for *rkr*). (B) Paired-pulse ratio (the 2nd EPSC amplitude / the 1st EPSC amplitude) of PF-EPSCs are plotted as a function of the paired-pulse interval. Note that difference between normal (blue open symbol) and *rkr* (red filled symbol) mice were not statistically significant in all the intervals when tested by repeated ANOVA. (C) Representative traces of CF-EPSCs evoked by paired-pulse stimulation (50 ms interval). The traces are normalized to the peaks of the first EPSC (right, blue trace for normal, red trace for *rkr*). (D) Paired-pulse ratios of CF-EPSCs are plotted as a function of paired-pulse interval.. Note that difference between the normal (open circle) and *rkr* (filled circle) mice were not statistically significant when tested by repeated ANOVA. Each point represents the mean ± SEM

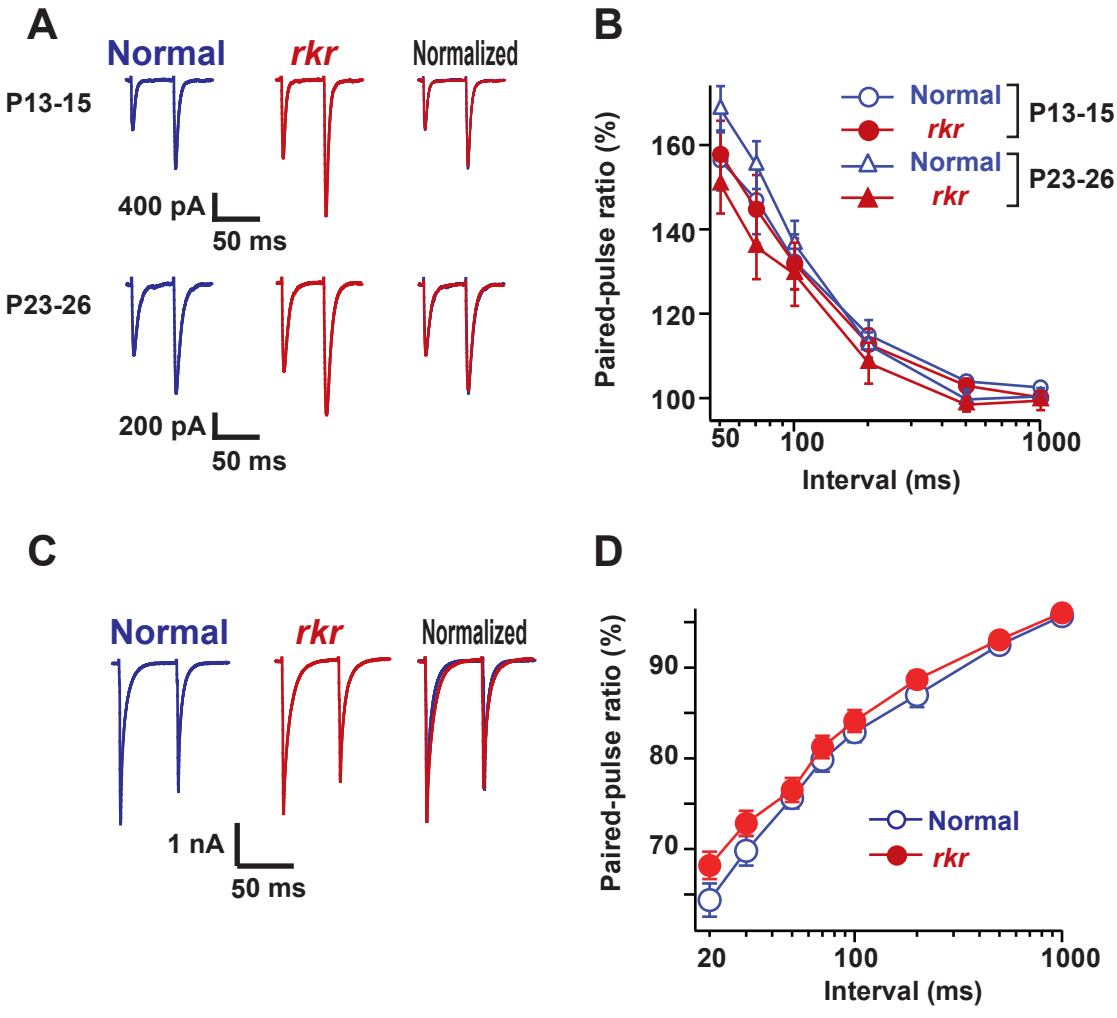
A
Normal
rkr
Normalized
P13-15
400 pA
50 ms
P23-26
200 pA
50 ms
B
Normal
rkr
P13-15
Normal
rkr
P23-26
Paired-pulse ratio (%)
160
140
120
100
50
100
1000
Interval (ms)
C
Normal
rkr
Normalized
1 nA
50 ms
D
Paired-pulse ratio (%)
90
80
70
Normal
rkr
20
100
1000
Interval (ms)

Fig. 3

Figure 4.

Basic properties of transmitter release at the PF-PC synapses in *rkr* mice. (A) Representative traces of PF-EPSCs in the presence of 1 or 3 mM $[Ca^{2+}]_e$ (thick line) are overlaid with control traces recorded in the presence of 2 mM $[Ca^{2+}]_e$ (thin line). All traces are normalized to the peaks of control EPSCs (dashed lines). (B) PF-EPSC amplitudes are plotted as a function of $[Ca^{2+}]_e$. The current amplitudes are normalized to those at 2 mM $[Ca^{2+}]_e$. Note that difference between normal (open circle) were *rkr* (filled circle) mice were not statistically significant when tested by unpaired *t*-test. (C) Representative traces of PF-EPSCs in the presence of 1 mM γ-DGG (thick line) are overlaid with control traces (thin line). All traces are normalized to the peaks of control EPSCs (dashed line). (D) The blockade of γ-DGG on PF-EPSCs, showing no significant difference (n.s.) between normal (open bar, n = 3) and *rkr* (gray bar, n = 5) mice when tested by unpaired *t*-test. All error bars represent SEM.

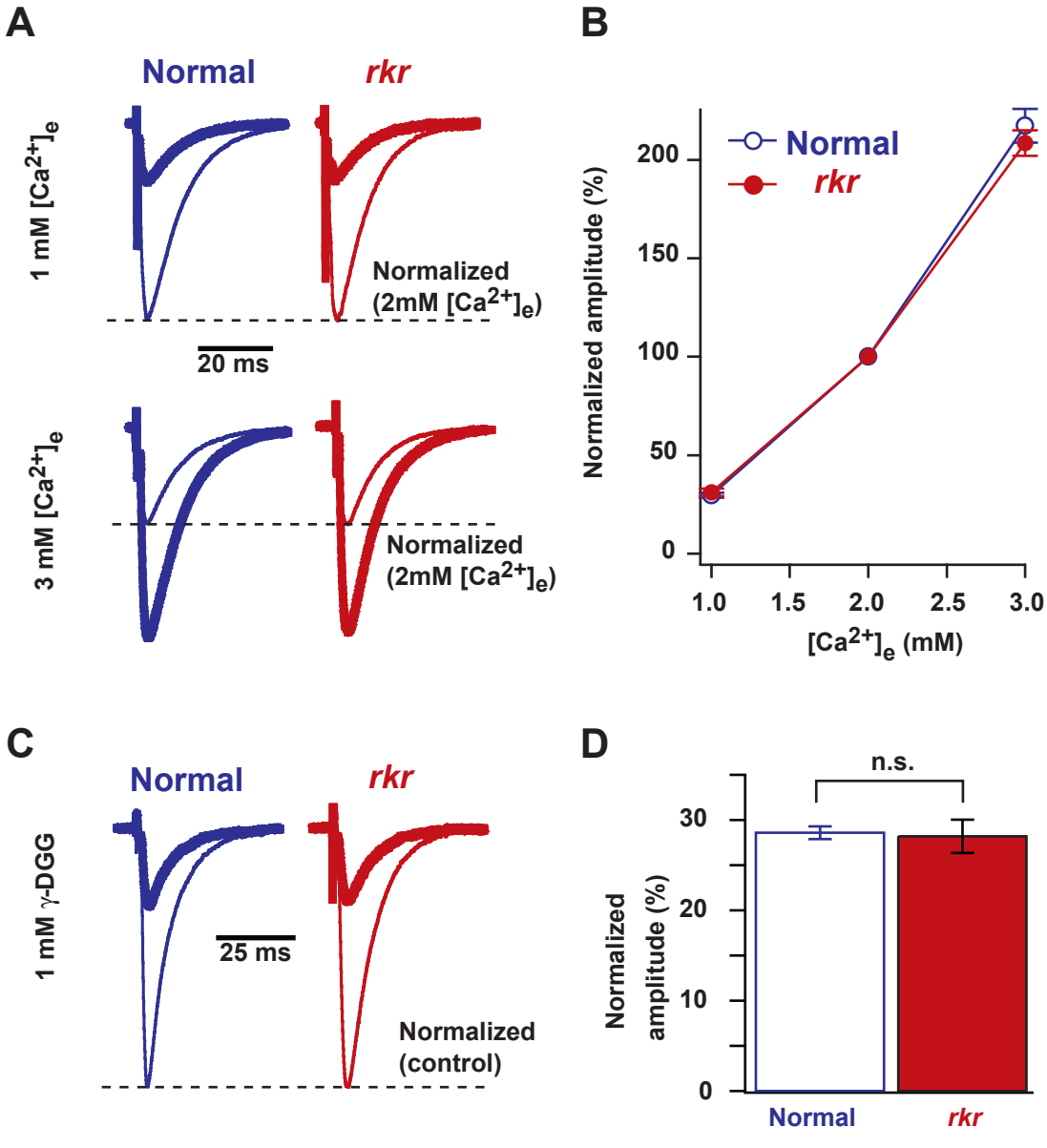
A
Normal
rkr
1 mM [Ca2+]e
Normalized
(2mM [Ca2+]e)
20 ms
3 mM [Ca2+]e
Normalized
(2mM [Ca2+]e)
B
Normal
rkr
Normalized amplitude (%)
200
150
100
50
0
1.0
1.5
2.0
2.5
3.0
[Ca2+]e (mM)
C
Normal
rkr
1 mM γ-DGG
25 ms
Normalized
(control)
D
n.s.
Normalized
amplitude (%)
30
20
10
0
Normal
rkr

Fig. 4

Figure 5.

Raw representative electron micrographs of replicas labeled with immunogold particles (top; 5 nm for AMPA receptors, 15 nm for GluRδ2), and illustrations for IMP clusters (red) and immunogold particles belonging to them (blue) (bottom).

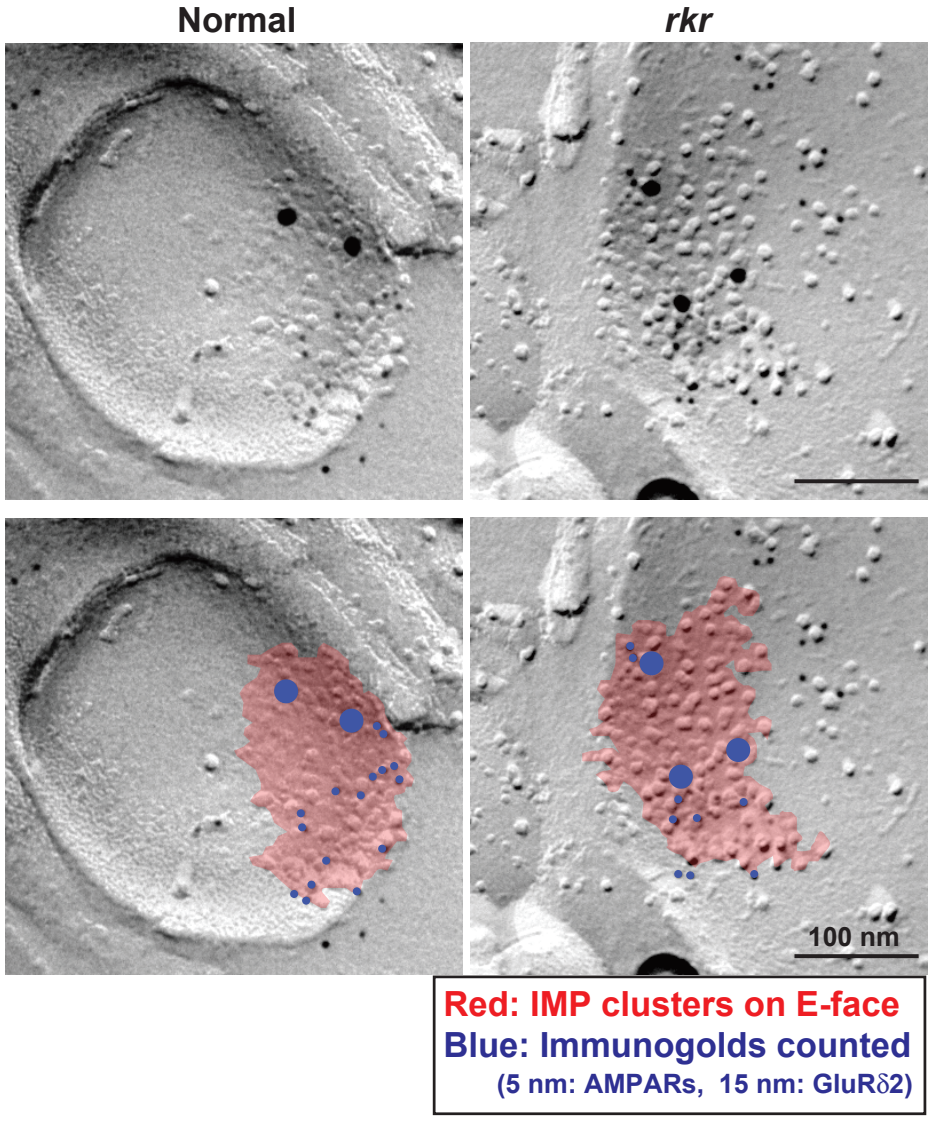
Normal
rkr
100 nm
Red: IMP clusters on E-face
Blue: Immunogolds counted
(5 nm: AMPARs, 15 nm: GluRδ2)

Fig. 5

Figure 6.

The density of immunogold particles for postsynaptic AMPA receptors in the PF-PC synapses revealed by SDS-FRL. (A and B) Distribution of the density of immunogold labels for AMPA receptors (A) and GluRδ2 (B). Comparison of the histograms for normal (blue, n = 300) and *rkr* (red, n = 284) mice (top) demonstrates selective reduction of the density of the labels for AMPA receptors in *rkr* mice. (C and D) The cumulative conversion of the histograms for the density of the AMAP receptor labels (C), and the GluRδ2 labels (D). The reduced density of AMPA receptor labels is apparent in (C), and statistically significant when tested by Mann-Whitney U-test (*** $p < 0.001$). Mean ± SD (unit: particles/μm^2) and coefficient of variance (c.v.) are indicated in inset.

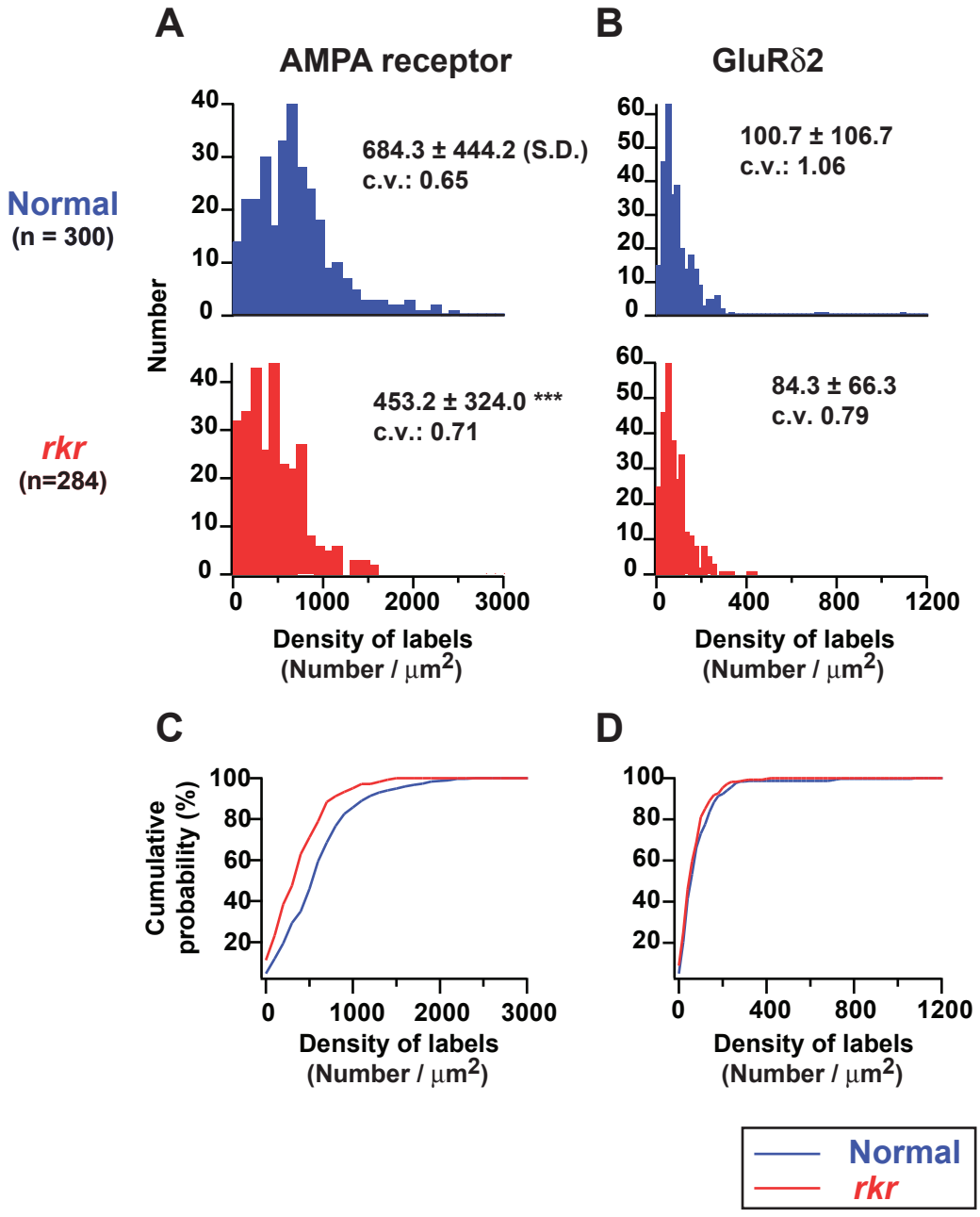
A
AMPA receptor
B
GluRδ2
Normal
(n = 300)
rkr
(n=284)
Number
684.3 ± 444.2 (S.D.)
c.v.: 0.65
100.7 ± 106.7
c.v.: 1.06
453.2 ± 324.0 ***
c.v.: 0.71
84.3 ± 66.3
c.v. 0.79
Density of labels
(Number / μm2)
C
D
Cumulative probability (%)
Normal
rkr

Fig. 6

Figure 7.

Raw representative electron micrographs of complete synapse replicas. Illustrations are the same as in *Figure 5*.

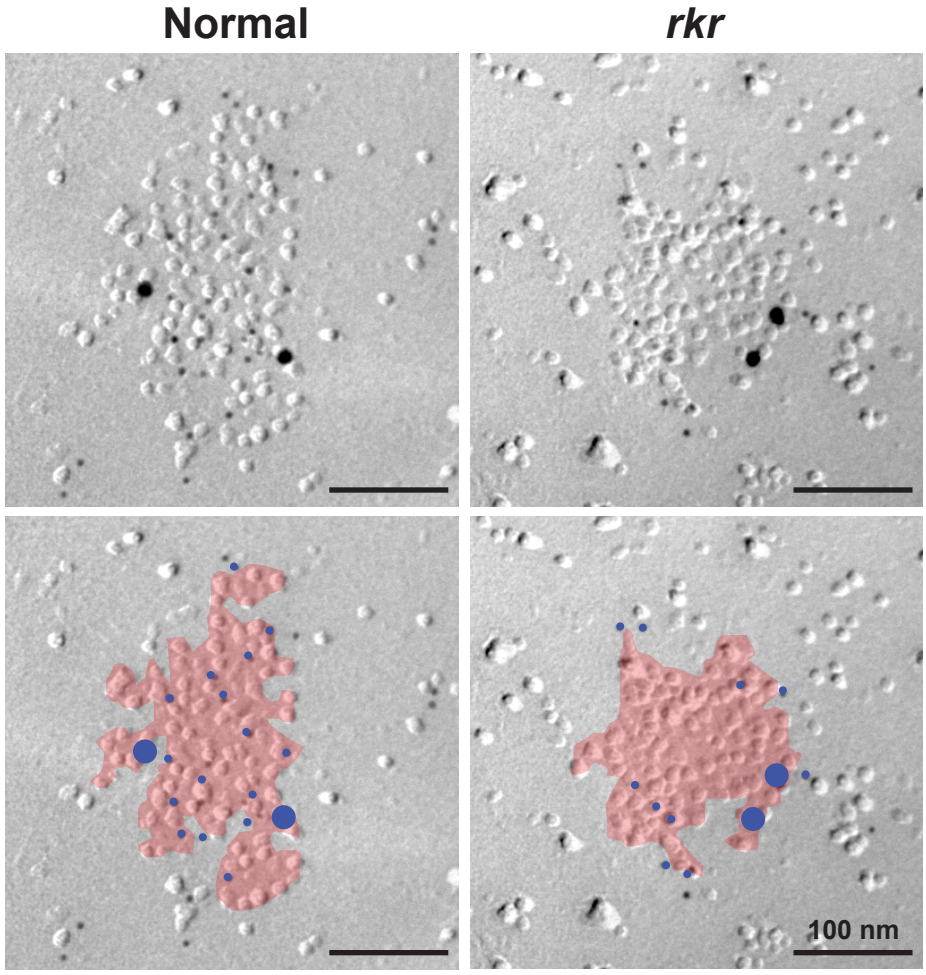

Red: IMP clusters on E-face
Blue: Immunogolds counted
(5 nm: AMPARs, 15 nm: GluRδ2)

Fig. 7

Figure 8.

The results of the quantifications on complete synapse replica of the PF-PC synapses. (A, B and C) Distribution of the total number of immunogold labels for AMPA receptors (A) and GluRδ2 (B) within a IMP cluster of a complete synapse ,and area of IMP clusters of complete synapses (C). Comparison of the histograms for normal (blue, n = 68 synapses) and *rkr* (red, n = 74 synapses) mice demonstrates selective reduction of the total number of the labels for AMPA receptors, and normal size of IMP clusters in *rkr* mice. (D,E and F) The cumulative conversion of the histograms for the total number of the AMAP receptor labels (D), and the GluRδ2 labels (E), and for the area of IMP clusters (F). The selective reduction of the total number of the AMPA receptor labels is apparent in (D), and statistically significant when tested by Mann-Whitney U-test (*** $p < 0.001$).

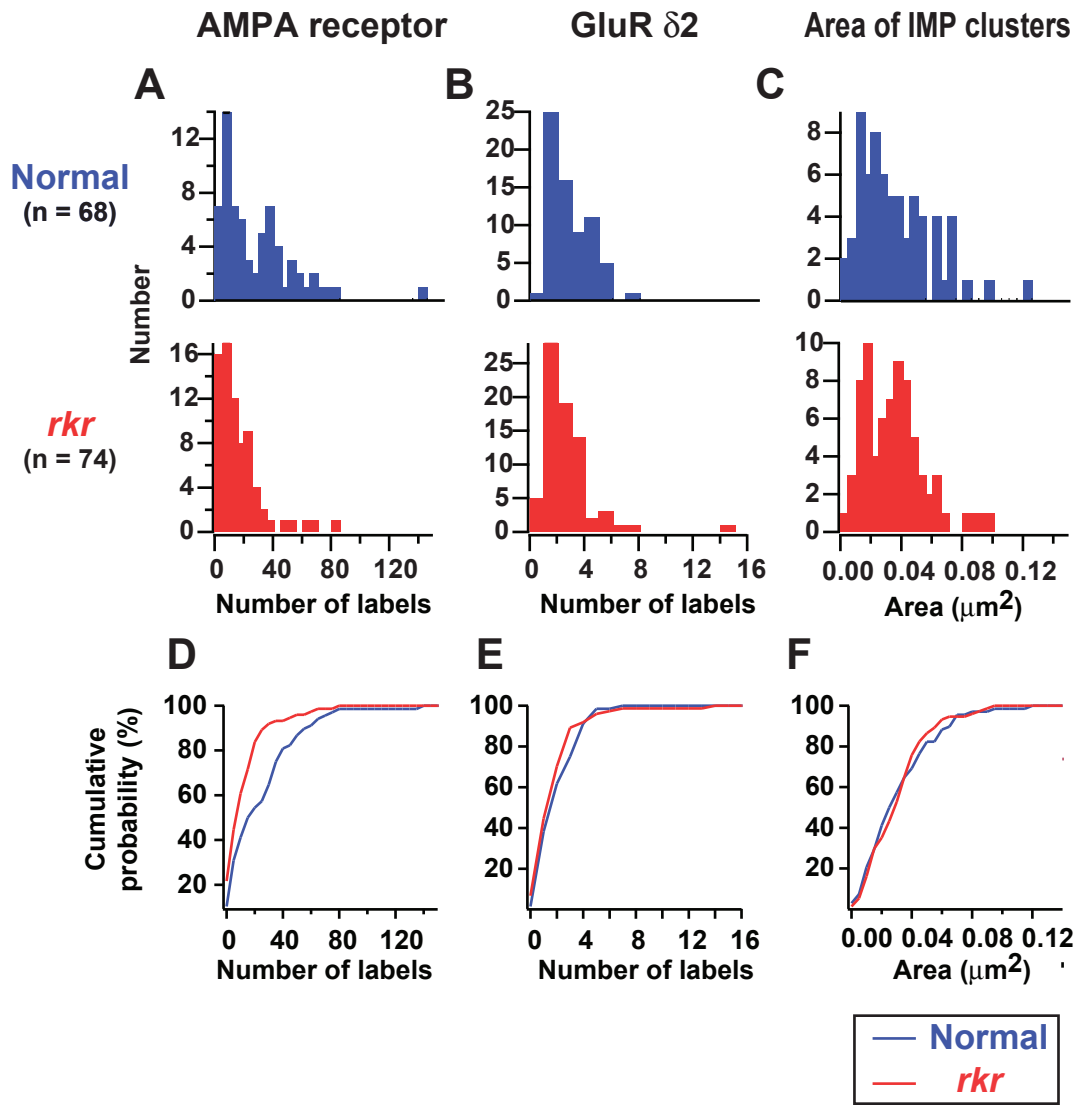
AMPA receptor
GluR δ2
Area of IMP clusters
A
B
C
Normal
(n = 68)
rkr
(n = 74)
Number
Number of labels
Number of labels
Area (μm2)
D
E
F
Cumulative probability (%)
Number of labels
Number of labels
Area (μm2)
Normal
rkr

Fig. 8

Figure 9.

Electron microscopic reconstruction of the PF-PC synapses and measurement of PSD area. (A) Representative images of electron micrographs from serial ultrathin sections (60 nm thick). (B) Distribution of the PSD area measured in the reconstructed PF-PC synapses. (C) The cumulative conversion of the histograms in (B). There was no statistical significance when tested by Mann-Whitney U-test.

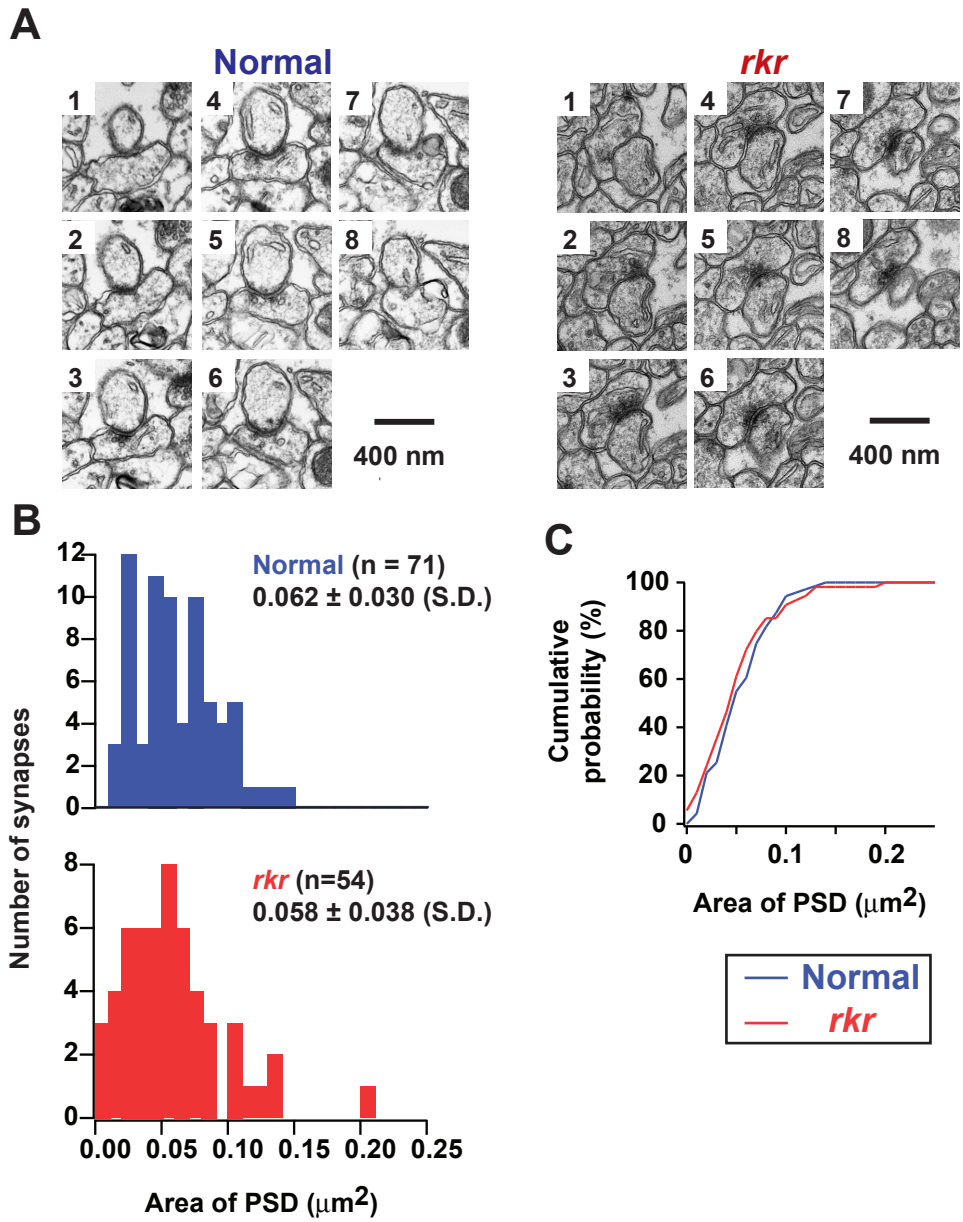
A
Normal
rkr
1
2
3
4
5
6
7
8
400 nm
400 nm
B
Normal (n = 71)
0.062 ± 0.030 (S.D.)
rkr (n=54)
0.058 ± 0.038 (S.D.)
Number of synapses
Area of PSD (μm2)
C
Cumulative probability (%)
Area of PSD (μm2)
Normal
rkr

Fig. 9

Figure 10.

Quantification of the density of the PF-PC synapses per PC in the ML. (A and B) Representative images of immunostaining against calbindin, which resulted in selective staining of PCs in cerebellum from normal (A) and *rkr* (B) mice. (C) Quantitative comparison of the density of PCs. There was no statistical significance when tested by unpaired *t*-test. (D and E) Distribution of the density of PF-PC synapses in the upper ML region from normal (D) and *rkr* (E) mice, which was measured by physical disector on serial electron micrographs. (C) The cumulative conversion of the histograms in (D) and (E). There was no significant difference when tested by unpaired *t*-test.

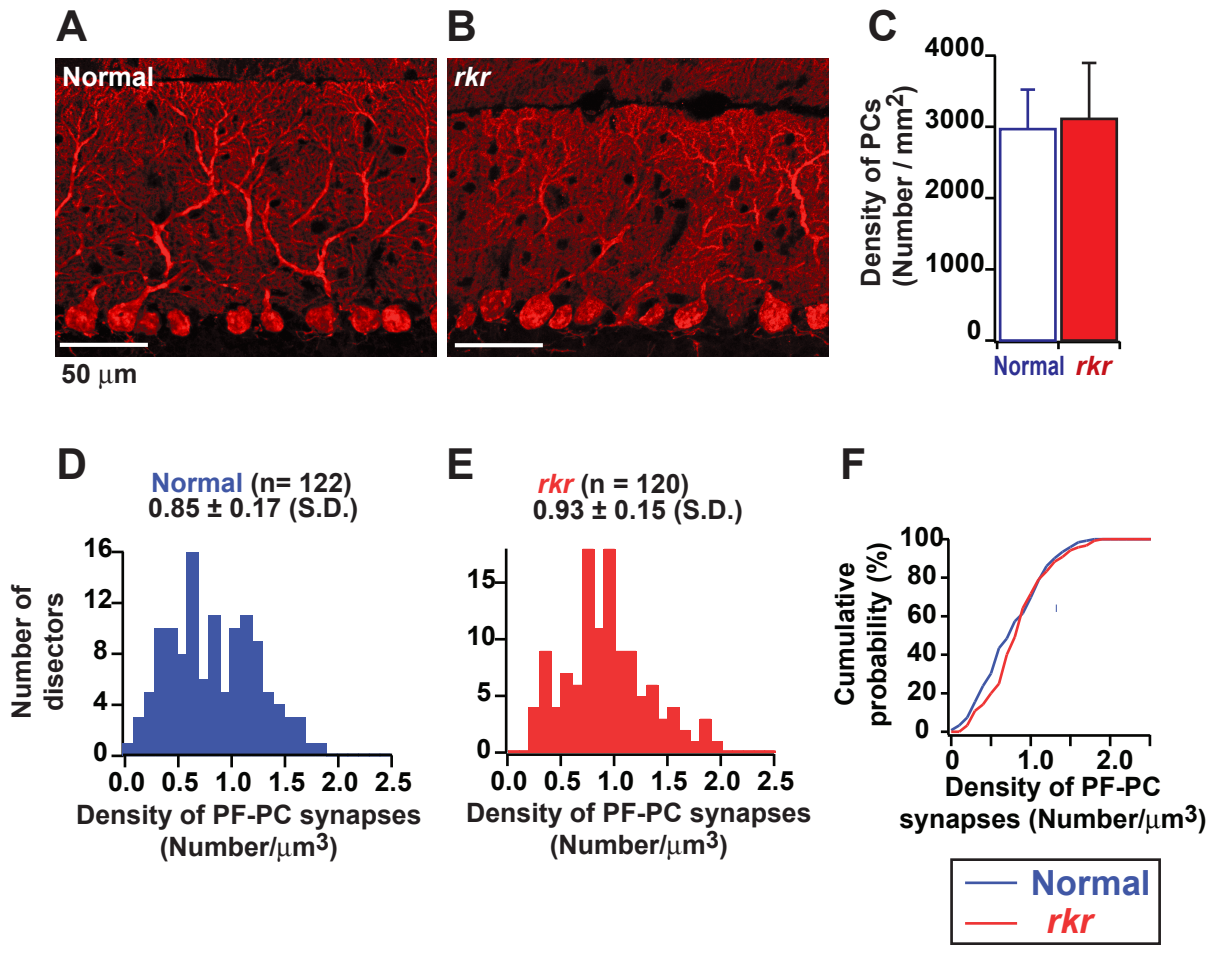
A
Normal
B
rkr
50 μm
C
Density of PCs (Number / mm2)
4000
3000
2000
1000
0
Normal
rkr
D
Normal (n= 122)
0.85 ± 0.17 (S.D.)
Number of disectors
16
12
8
4
0
0.0 0.5 1.0 1.5 2.0 2.5
Density of PF-PC synapses (Number/μm3)
E
rkr (n = 120)
0.93 ± 0.15 (S.D.)
15
10
5
0
0.0 0.5 1.0 1.5 2.0 2.5
Density of PF-PC synapses (Number/μm3)
F
Cumulative probability (%)
100
80
60
40
20
0
0
1.0
2.0
Density of PF-PC synapses (Number/μm3)
Normal
rkr

Fig. 10

Figure 11.

Projection images of the PCs from normal (A; blue) and *rkr* (B; red) mice. These were retrogradely labeled with biotinylated dextran amine, and visualized fluorescently with Alexa Fluor 488. Images were obtained by confocal laser scanning microscopy and digitally processed to remove noise. All PCs analyzed are shown.

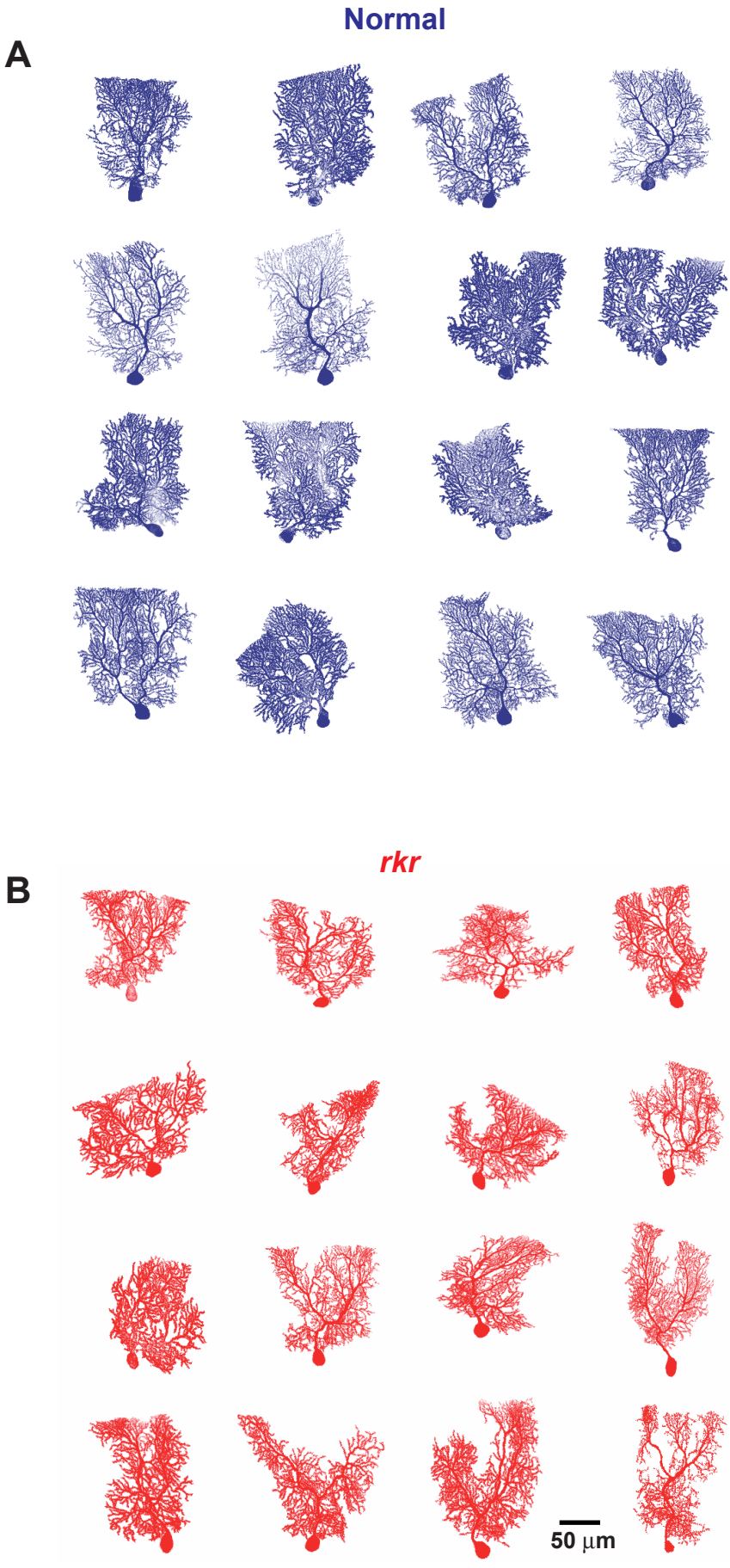

Fig. 11

of the spine density on the most distal dendrites of PCs (n = 14 dendrites, 9 cells, 3 animals for normal mice, 274.7 μm analyzed in total; n = 15 dendrites, 8 cells, 3 animals for *rkr* mice, 274.1 μm analyzed in total), showing no statistical difference (n.s.). * $p < 0.05$, ** $p < 0.01$, *** $p < 0.001$.

Figure 12.

Morphometric assessment of the abnormal dendritic branching in *rkr* PCs. (A) Illustration of the method to quantify the complexity of arborization by the number of times that the dendrites crossed the evenly spaced lines that are parallel to the pia. 0 and 100% of ML level are corresponded to the apical boundary line of soma of PCs, and the pia, respectively. (B) Distribution of the number of dendrites crossings the lines. Normal PCs (open blue circle, n = 16 cells) showed rich branching of dendrites in the region of the ML close to the pia, whereas the dendrites of *rkr* PCs (filled red circle, n = 16 cells) arborized less there. Statistical test revealed significant difference in their arborization in some ML levels when tested by repeated ANOVA followed by Bonferroni test. (C) Illustration of the method to quantify the content of PC dendrites per area of the upper ML. A semicircle is placed adjacent to the pia and moved laterally along the pia to find the position where the total length of dendrites contained within becomes maximal. (D) Quantitative comparison of the maximal content of PC dendrites per area of the upper ML (open blue circle for normal mice, n = 16 cells; filled red circle for *rkr* mice, n = 16 cells). With the semicircles of 70 μm and 90 μm-diameter, significant reductions were observed in *rkr* mice, when tested by repeated ANOVA followed by Bonferroni test. (E) Projection images of the most distal dendrites of the PCs. (F) Quantitative comparison

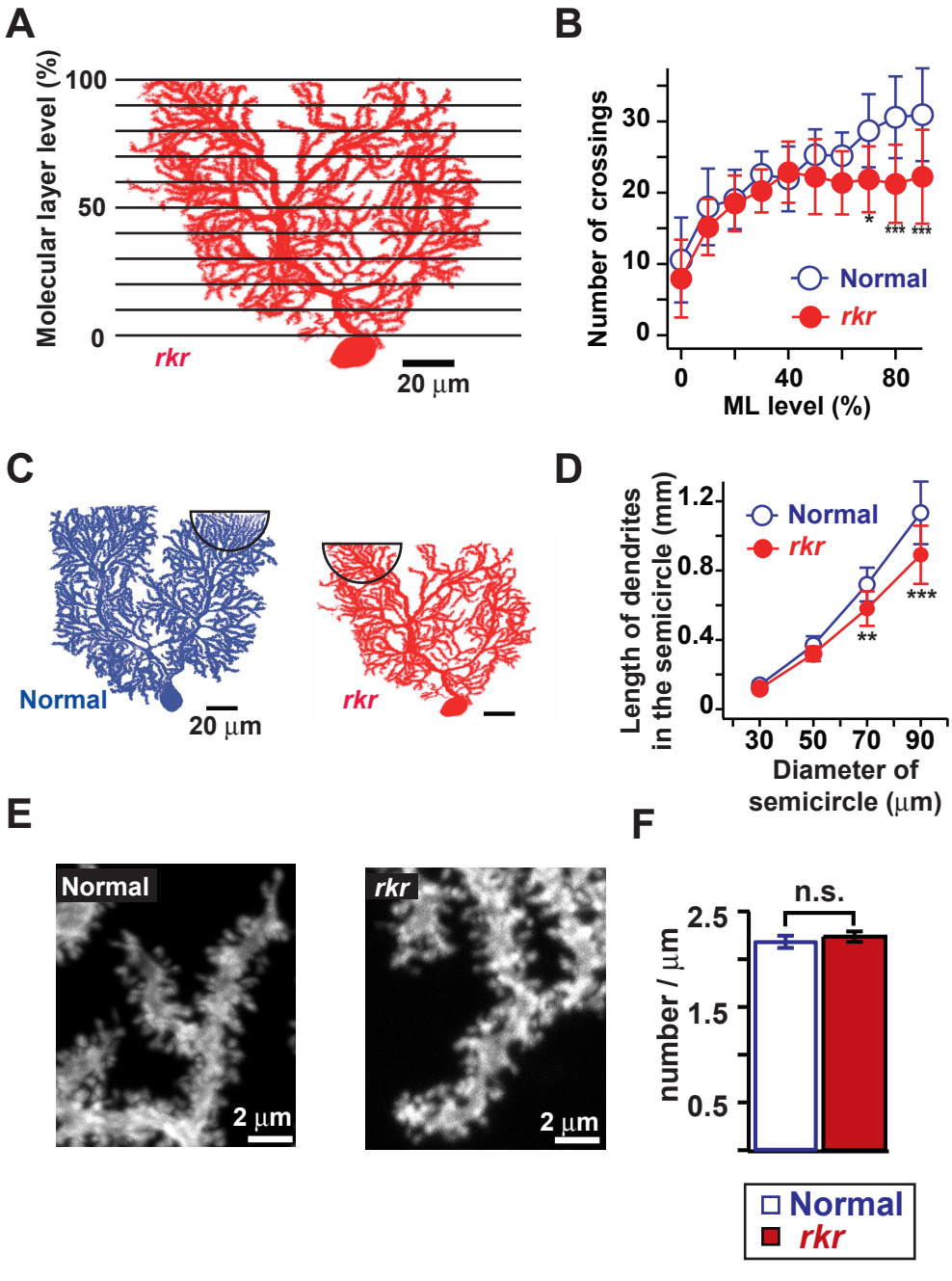
A
Molecular layer level (%)
100
50
0
rkr
20 μm
B
Number of crossings
30
20
10
0
0
40
80
ML level (%)
Normal
rkr
*
***
***
C
Normal
20 μm
rkr
D
Length of dendrites in the semicircle (mm)
1.2
0.8
0.4
0
30
50
70
90
Diameter of semicircle (μm)
Normal
rkr
**
***
E
Normal
2 μm
rkr
2 μm
F
n.s.
number / μm
2.5
1.5
0.5
Normal
rkr

Fig. 12

Figure 13.

Example data of PC firing in vivo. (A and B) Extracellular recording of spontaneous PC activities of normal (A) and *rkr* (B) mice under urethane anesthesia. Note the increased irregularity of the simple spikes in *rkr*. * indicates a complex spike. (C and D) Autocorrelations during spontaneous firing show that the periodicity of simple spikes in normal mice (C) was much better than that in *rkr* mice (D). Peaks at 0 sec are truncated by expansion. Autocorrelograms were calculated from 20 s of recording data with ±1 ms of spike match window and 2 ms of sliding step. (E) Experimental illustrations of in vivo recording of neural activities in response to somatosensory stimulation (an air puff to the perioral skin). (F) Representative data of the response to the air puff stimulations recorded from a PC in cerebellar crus I of normal mice. The discharge rate of simple spikes (blue) was decreased in response to the stimulation, whereas that of complex spikes (red) was increased.

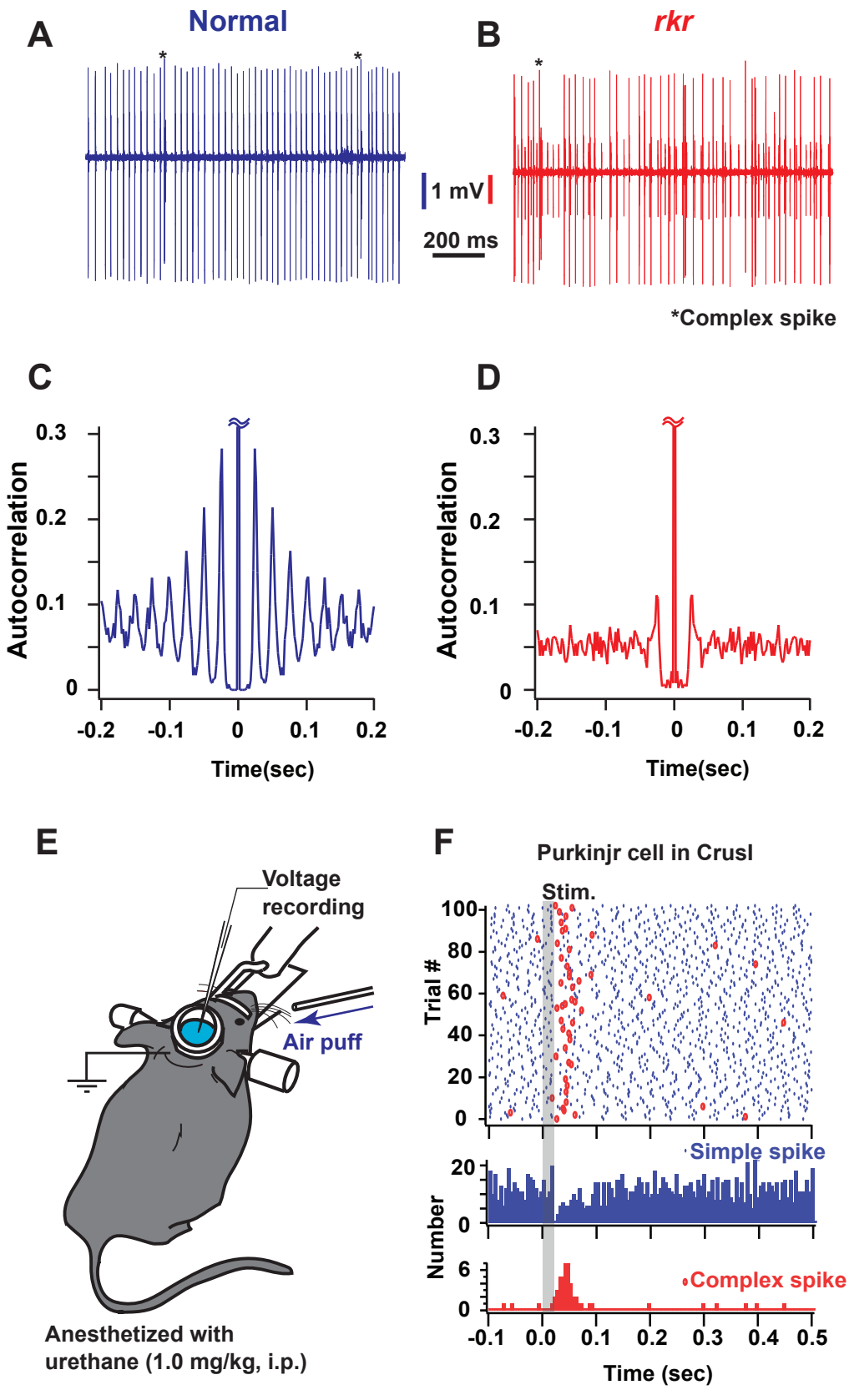
A
Normal
B
rkr
1 mV
200 ms
*Complex spike
C
D
Autocorrelation
0.3
0.2
0.1
0
-0.2
-0.1
0
0.1
0.2
Time(sec)
E
Voltage recording
Air puff
Anesthetized with urethane (1.0 mg/kg, i.p.)
F
Purkinjr cell in Crusl
Stim.
Trial #
100
80
60
40
20
0
Simple spike
Number
20
0
6
0
Complex spike
-0.1
0.0
0.1
0.2
0.3
0.4
0.5
Time (sec)

Fig. 13

Basic properties of Parallel fiber -> Purkinje cell EPSCs

	Amplitude (nA)	Decay time constant (ms)	10-90% Rise time (ms)
Mice(P13-15)			
Normal	1.51±0.14 (11)	4.34±0.36 (11)	1.26±0.18 (10)
rkr	0.80±0.14 ** (12)	4.72±0.28 (17)	1.13±0.19 (10)
Mice(P23-26)			
Normal	1.24±0.12 (8)	8.70±1.17 (11)	2.12±0.19 (10)
rkr	0.38±0.07 *** (11)	9.16±0.08 (11)	1.69±0.09 (9)

The amplitude of PF-EPSC is measured at stimulation of 17.5 μA. All data are expressed as mean ± SEM. Number of the recorded Purkinje cells are shown in parentheses. The decay time constant is obtained by fitting the EPSC decay with a single exponential. Paired-pulse ratio is second EPSC / first EPSC at interpulse interval of 50 ms.** $p < 0.01$, *** $p < 0.001$

Basic properties of climbing fiber -> Purkinje cell EPSCs

	Chord conductance (nS)	Decay time constant (ms)	10-90% Rise time (ms)	Paired pulse ratio (%)
Mice(P22-30)				
Normal	211.8±18.9 (20)	4.02±0.21 (21)	0.52±0.02 (21)	75.6±1.2 (22)
rkr	140.0±12.4** (23)	6.20±0.46 ***(22)	0.48±0.02 (21)	76.5±1.3 (25)

All data are expressed as mean ± SEM. Number of the recorded Purkinje cells are shown in parentheses. The decay time constant is obtained by fitting the EPSC decay with a single exponential. Paired-pulse ratio is second EPSC / first EPSC at interpulse interval of 50 ms.** $p < 0.01$, *** $p < 0.001$.

Table 1

Synaptic abnormalities in $Ca_V2.1$ mutant mice

		severe ← Ataxia → moderate			
		KO (1)	***rol*** (2)	***tg*** (2)	***rkr***
PF-PC synapses	EPSC amplitude reduction	***N.D.***	+++	+++	+++
	EPSC kinetics	-	-	-	-
	Paired-pulse ratio change	+(↑)	+(↑)	-	-
	Progressive impairment	***N.D.***	***N.D.***	+	+
CF-PC synapses	Conductance change	-	+(↑)	-	+(↓)
	EPSC kinetics	Slower rise & decay	Slower decay	-	Slower decay
	Paired-pulse ratio change	+(↓)	-	+(↑)	-
	CF multiple innervation	+++	+?	***N.D.***	-

KO; $Ca_V2.1$ knockout, *rol*; *rolling*, *tg*; *tottering*, *rkr*; *rocker*

(1) Miyazaki, T., Hashimoto, K., Shin, H. -S., Kano, M. & Watanabe, M. (2004) P/Q-type Ca^{2+} channel α1A regulates synaptic competition on developing cerebellar Purkinje cells. *J. Neurosci.*, **24**, 1734-1743

(2) Matsushita, K., Wakamori, M., Rhyu, I. J., Arii, T., Oda, S., Mori, Y. & Imoto, K. (2002) Bidirectional alterations in cerebellar synaptic transmission of *tottering* and *rolling* Ca^{2+} channel mutant mice. *J. Neurosci.*, **22**, 4388-4398

Table 2